

Calculating Vacuum Energies in Renormalizable Quantum Field Theories: A New Approach to the Casimir Problem

N. Graham^a, R.L. Jaffe^b, V. Khemani^b, M. Quandt^b, M. Scandurra^b, H. Weigel^{1b,c}

^aDepartment of Physics and Astronomy,
University of California, Los Angeles
Los Angeles, CA 90095

^bCenter for Theoretical Physics, Laboratory for Nuclear Science
and Department of Physics, Massachusetts Institute of Technology
Cambridge, Massachusetts 02139

^cInstitute for Theoretical Physics, Tübingen University
D-72076 Tübingen, Germany

UCLA/02/TEP/14

MIT-CTP-3278
hep-th/0207120

UNITU-HEP-11/2002

Abstract

The Casimir problem is usually posed as the response of a fluctuating quantum field to externally imposed boundary conditions. In reality, however, no interaction is strong enough to enforce a boundary condition on all frequencies of a fluctuating field. We construct a more physical model of the situation by coupling the fluctuating field to a smooth background potential that implements the boundary condition in a certain limit. To study this problem, we develop general new methods to compute renormalized one-loop quantum energies and energy densities. We use analytic properties of scattering data to compute Green's functions in time-independent background fields at imaginary momenta. Our calculational method is particularly useful for numerical studies of singular limits because it avoids terms that oscillate or require cancellation of exponentially growing and decaying factors. To renormalize, we identify potentially divergent contributions to the Casimir energy with low orders in the Born series to the Green's function. We subtract these contributions and add back the corresponding Feynman diagrams, which we combine with counterterms fixed by imposing standard renormalization conditions on low-order Green's functions. The resulting Casimir energy and energy density are finite functionals for smooth background potentials. In general, however, the Casimir energy diverges in the boundary condition limit. This divergence is real and reflects the infinite energy needed to constrain a fluctuating field on all energy scales; renormalizable quantum field theories have no place for ad hoc surface counterterms. We apply our methods to simple examples to illustrate cases where these subtleties invalidate the conclusions of the boundary condition approach.

Keywords: Energy densities, Green's functions, density of states, renormalization, Casimir effect

PACS: 03.65.Nk, 03.70.+k, 11.10.Gh

¹Heisenberg Fellow

1. Introduction

Long ago, Casimir predicted the existence of a force generated by quantum fluctuations of the electromagnetic field between uncharged, perfectly conducting metal plates in vacuo [1]. Since then, many related calculations have been carried out (for reviews see [2, 3, 4, 5, 6]). The standard approach to problems of this type has been to consider the response of a free quantum field to time-independent boundary conditions imposed on stationary surfaces. This calculation is an idealization of the more physical description of the quantum field as interacting with a smooth external potential, which goes to zero away from the surfaces. This paper will provide the technical tools necessary for understanding precisely when this idealization is justified, and when it is hazardous. We will demonstrate the use of these tools in some simple models; the reader is also referred to [7] for a briefer, less technical, and more focused discussion of a variety of Casimir problems.

In the field theory picture, the dynamics of a fluctuating field in a background potential is governed by the one-loop effective energy, which can be expressed either as an infinite sum of Feynman diagrams or as a “Casimir sum” over modes. Both expressions are formally divergent, so they can only be defined by introducing counterterms fixed with physical renormalization conditions. A Dirichlet boundary condition emerges when a repulsive background scalar field becomes strong and sharply peaked. We will see that the renormalized total energy of the fluctuating field relative to its value in the absence of boundaries can diverge in this limit. In such cases, the idealized Casimir energy *per se* does not exist. However, these divergences are associated with the boundaries and therefore do not affect the energy density away from the boundaries or the force between rigid surfaces. Nevertheless some geometric quantities, such as the “Casimir stress” [8] — the force per unit area on the surface where the boundary conditions are applied — are sensitive to these divergences. In such cases, there is no way to calculate meaningful finite results by considering boundary conditions.

To demonstrate these results in detail, we require efficient and robust techniques for computing Casimir energies and energy densities, which we describe in Section 2. The calculation of Casimir energy densities is interesting in its own right, for example in the study of energy conditions in general relativity [2, 9, 10]. Our approach will phrase the calculation in the language of conventional renormalizable quantum field theory, in a way that is amenable to efficient numerical computation. We study the vacuum polarization energy and energy density of a fluctuating boson field ϕ coupled to a background $\sigma(\vec{x})$, which is sharply peaked in the boundary condition limit. We introduce counterterms fixed by perturbative renormalization conditions, which define physical inputs to the theory such as particle masses and coupling constants at particular values of the external momenta. The resulting renormalization scheme is conventional, precise, and unambiguous. It can be related to any another conventional scheme by the analysis of low-order Feynman diagrams. We do not, however, see any relation between this scheme and analyses in which boundary surface dependent counterterms are introduced in an *ad hoc* manner. It is a common procedure in the literature to simply ignore divergent surface integrals and pole terms arising in the course of the calculation [11, 12]. The ζ -function method, in particular, introduces counterterms of any power of the geometrical parameter [13]. Such counterterms redefine classical parameters

of the background, but have no justification in quantum field theory. As a result, these approaches do not appear to be reconcilable with ordinary renormalizable quantum field theory.

Our method is based on an extension of methods developed for the total energy [14, 15], together with an extension of the analytic continuation methods introduced in Ref. [16]. First, we relate the matrix element of the energy density operator to the scattering Green's function at coincident points, $G(\vec{x}, \vec{x}, k)$. We regulate the large k behavior of G by subtracting the first few terms in its Born expansion and adding back the contribution of the associated low-order Feynman diagrams [14, 15]. The Green's function is difficult to deal with at large (real) k when the background field approaches the boundary condition limit: it oscillates with amplitude much larger than the net contribution to the energy density. To avoid such oscillations we rotate k to the imaginary axis [16, 17]. Before doing so, however, we rewrite the Green's function as a product of terms, each of which is bounded for k on the imaginary axis and each of which can be easily computed by integrating a Schrödinger-like equation subject to simple boundary conditions. This formalism allows us to avoid exponentially growing quantities anywhere in the calculation. As a result, we are able to write the Casimir energy density as an integral along the positive imaginary axis and perform the integral directly for imaginary k . Here we depart from Refs. [16, 17], which formulate the problem as an integral along the imaginary axis but then use a dispersion relation to compute the integrand in terms of scattering data for real k .

The final ingredient we need for the calculation is the Feynman diagram contribution, which is where we implement the renormalization conditions. The energy density operator \hat{T}_{00} generates insertions in Feynman diagrams of every order in the background field σ . Using a functional approach allows us to keep careful track of orders in σ in this calculation, which we need to maintain consistency with the rest of the calculation.

In Section 3 we show how to apply our methods to a simple example, the Casimir energy density for a boson field in one space dimension. We couple the fluctuating field ϕ to a background $\sigma(x)$ with an interaction of the form $\lambda\phi^2\sigma(x)$. For $\sigma(x) = \delta(x-a) + \delta(x+a)$, we obtain Dirichlet boundary conditions at $x = \pm a$ in the limit where the coupling constant λ becomes infinite. We find that the *total* Casimir energy diverges in this limit. The divergence is localized at the points where the background σ is nonzero. For all $x \neq \pm a$, the energy density remains finite and as λ approaches infinity it smoothly approaches the result obtained by imposing the boundary condition $\phi = 0$ at $x = \pm a$. To complete Section 3 we study the vacuum polarization energy in the presence of a smooth, strongly peaked background field. By taking σ to be the sum of Gaussians centered at $\pm a$, we can study the way that the energy density behaves as $\sigma(x)$ approaches the boundary condition limit. As expected, it approaches its limiting form at every $x \neq \pm a$, though the rate of approach depends on the proximity to $\pm a$.

In Section 4 we consider the case of a circle in two spatial dimensions. We consider Gaussian backgrounds peaked around $r = a$ and study the limit in which the Gaussian approaches a δ -function. When the strength of the coupling goes to infinity, we obtain a Dirichlet boundary condition at $r = a$. However, the renormalized total energy diverges in the δ -function limit, even at finite coupling. This result is a simple consequence of the

fact that $\int d^2x [\sigma(r)]^2 \rightarrow \infty$ in this limit. As a result, the surface tension on the circle — the derivative of the energy with respect to a — diverges. This example illustrates the generic problem we have found with attempts to define the Casimir energy in the context of a quantum field theory: Even though the renormalized vacuum polarization energy is a finite functional of a smooth background, it diverges as the background field assumes the singular configuration necessary to implement the boundary condition. This divergence affects any physical quantity, such as the surface tension, whose measurement requires comparison of configurations with different boundaries, for which the divergent contributions are different. We take this divergence as an indication that such quantities depend on the details of the interaction between the fluctuating field and the material to which it couples. Thus the Casimir stress cannot be defined in a way that is independent of the other stresses to which the material is subject.

We close with a summary and some considerations for future work in Section 5 and give technical details in the Appendices.

2. Method

We begin by developing the method for computing the energy density of a fluctuating quantum field coupled to a classical background. From the corresponding scattering and bound state wavefunctions, we construct a Fock decomposition of the quantum field and compute the matrix element of the energy density operator \hat{T}_{00} . We express this matrix element in terms of a Green's function with appropriate boundary conditions. The energy density is given by a sum over bound states plus an integral over the continuum labeled by the wave number k . We develop a representation of the Green's function suitable for analytic continuation into the upper half k -plane, so the k integral can be deformed along a cut on the positive imaginary axis. To regulate the ultraviolet divergences of the theory, which corresponds to eliminating the contribution associated with the semi-circle at infinite complex momenta, we subtract leading Born approximations to the Green's function, which we later add back in as Feynman diagrams. These diagrams are then regularized and renormalized in ordinary Feynman perturbation theory.

2.1 Formalism

We consider a static, spherically symmetric background potential $\sigma = \sigma(r)$ with $r = |\vec{x}|$ in n spatial dimensions. The symmetric energy density operator for a real scalar field coupled to σ is

$$\begin{aligned} \hat{T}_{00}(x) &= \frac{1}{2} \left[\dot{\phi}^2 + (\vec{\nabla}\phi)^2 + m^2\phi^2 + \sigma(r)\phi^2 \right] \\ &= \frac{1}{2} \left[\dot{\phi}^2 + \phi \left(-\vec{\nabla}^2 + m^2 + \sigma(r) \right) \phi \right] + \frac{1}{4} \vec{\nabla}^2 (\phi^2) \end{aligned} \quad (1)$$

where we have rearranged the spatial derivative term in order to be able to use the Schrödinger equation to evaluate the expression in brackets. We assume that the background

potential is smooth, with $\int_0^\infty dr |\sigma(r)|(1+r) < \infty$.² We define the “vacuum” to be the state $|\Omega\rangle$ of lowest energy in the background σ and the “trivial vacuum” to be the state $|0\rangle$ of lowest energy when $\sigma \equiv 0$. The vacuum energy density is the renormalized expectation value of \hat{T}_{00} with respect to the vacuum $|\Omega\rangle$, $\langle \Omega | \hat{T}_{00}(x) | \Omega \rangle_{\text{ren}}$, which includes the matrix elements of the counterterms. Since we have spherical symmetry, we will define the energy density in a spherical shell,

$$\epsilon(r) = \frac{2\pi^{n/2}}{\Gamma(\frac{n}{2})} r^{n-1} \langle \Omega | \hat{T}_{00}(x) | \Omega \rangle_{\text{ren}}. \quad (2)$$

We first perform a partial wave decomposition using spherical symmetry,

$$\phi(t, \vec{x}) = \sum_{\{\ell\}} \phi_\ell(t, r) \mathcal{Y}_{\{\ell\}}(\hat{x}) \quad (3)$$

where $\mathcal{Y}_{\{\ell\}}(\hat{x})$ are the n -dimensional spherical harmonics $\{\ell\}$ refers to the set of all angular quantum numbers in n dimensions. The total angular momentum assumes integer values $\ell = 0, 1, 2, \dots$ in all dimensions except for $n = 1$, where $\ell = 0$ and 1 only, corresponding to the symmetric and antisymmetric channels respectively. We make the Fock decomposition

$$\begin{aligned} \phi_\ell(t, r) = & \frac{1}{r^{\frac{n-1}{2}}} \int_0^\infty \frac{dk}{\sqrt{\pi\omega}} \left[\psi_\ell(k, r) e^{-i\omega t} a_\ell(k) + \psi_\ell^*(k, r) e^{i\omega t} a_\ell^\dagger(k) \right] \\ & + \frac{1}{r^{\frac{n-1}{2}}} \sum_j \frac{1}{\sqrt{2\omega_j}} \left[\psi_{\ell_j}(r) e^{-i\omega_j t} a_{\ell_j} + \psi_{\ell_j}(r) e^{i\omega_j t} a_{\ell_j}^\dagger \right], \end{aligned} \quad (4)$$

which we have split into scattering states with $\omega = \sqrt{k^2 + m^2}$ and bound states with $\omega_j = \sqrt{m^2 - \kappa_j^2}$. Note that the latter wave functions are real. The vacuum $|\Omega\rangle$ is annihilated by all of the $a_\ell(k)$ and a_{ℓ_j} . The radial wavefunctions in eq. (4) are solutions to the Schrödinger-like equation

$$-\psi'' + \frac{1}{r^2} \left(\nu - \frac{1}{2} \right) \left(\nu + \frac{1}{2} \right) \psi + \sigma(r)\psi - k^2\psi = 0 \quad (5)$$

where

$$\nu = \ell - 1 + \frac{n}{2}. \quad (6)$$

In each channel, we normalize the wavefunctions to give the completeness relation

$$\frac{2}{\pi} \int_0^\infty dk \psi_\ell^*(k, r) \psi_\ell(k, r') + \sum_j \psi_{\ell_j}(r) \psi_{\ell_j}(r') = \delta(r - r') \quad (7)$$

which implies the orthonormality relations

$$\begin{aligned} \int_0^\infty \psi_{\ell_j}(r) \psi_{\ell_{j'}}(r) dr &= \delta_{jj'} && \text{for the bound states and} \\ \int_0^\infty \psi_\ell^*(k, r) \psi_\ell(k', r) dr &= \frac{\pi}{2} \delta(k - k') && \text{for the continuum states.} \end{aligned} \quad (8)$$

²In view of later applications with singular background fields, we can relax this condition to allow for all $\sigma(r)$ for which a scattering problem in the usual sense can be defined. However, some of the standard bounds on the asymptotics of Jost functions no longer hold for a non-smooth $\sigma(r)$, giving rise to the additional singularities discussed later.

For $\sigma \equiv 0$, the normalized wavefunctions are $\psi_\ell^{(0)}(k, r) = \sqrt{\frac{\pi}{2kr}} J_\nu(kr)$. With the above conventions and normalizations, the standard equal time commutation relations for the quantum field ϕ yield canonical commutation relations for the creation and annihilation operators, $[a_\ell(k), a_{\ell'}^\dagger(k')] = \delta(k - k')\delta_{\ell, \ell'}$ and $[a_{\ell j}, a_{\ell' j'}^\dagger] = \delta_{jj'}\delta_{\ell\ell'}$ while all other commutators vanish.

The vacuum expectation value of the energy density can now be computed by using eq. (4) in eq. (1). We obtain

$$\begin{aligned} \epsilon(r) = & \sum_\ell N_\ell \left[\int_0^\infty \frac{dk}{\pi} \omega \psi_\ell^*(k, r) \psi_\ell(k, r) + \sum_j \frac{\omega_j}{2} \psi_{\ell j}(r)^2 \right] \\ & + \frac{1}{4} D_r \sum_\ell N_\ell \left[\int_0^\infty \frac{dk}{\pi \omega} \psi_\ell^*(k, r) \psi_\ell(k, r) + \sum_j \frac{1}{2\omega_j} \psi_{\ell j}(r)^2 \right] - \epsilon^{(0)}(r) + \epsilon_{\text{CT}}(r). \end{aligned} \quad (9)$$

where $N_\ell = \frac{\Gamma(n+\ell-2)}{\Gamma(n-1)\Gamma(\ell+1)}(n+2\ell-2)$ is the degeneracy factor in the ℓ^{th} partial wave, $D_r = \frac{\partial}{\partial r} \left(\frac{\partial}{\partial r} - \frac{n-1}{r} \right)$, $\epsilon_{\text{CT}}(r)$ is the counterterm contribution, and $\epsilon^{(0)}(r)$ indicates the subtraction of the energy in the trivial vacuum, which is just given by evaluating the first integral with free wavefunctions $\psi_\ell^{(0)}(k, r)$. This subtraction corresponds to a renormalization of the cosmological constant.

We can identify the scattering state contribution with the Green's function by defining the local spectral density

$$\rho_\ell(k, r) \equiv \frac{k}{i} G_\ell(r, r, k), \quad (10)$$

in the upper half-plane, so that for real k

$$\text{Re} \{ \rho_\ell(k, r) \} = \psi_\ell^*(k, r) \psi_\ell(k, r) = \text{Im} \{ k G_\ell(r, r, k) \}, \quad (11)$$

where

$$G_\ell(r, r', k) = -\frac{2}{\pi} \int_0^\infty dq \frac{\psi_\ell^*(q, r) \psi_\ell(q, r')}{(k+i\epsilon)^2 - q^2} - \sum_j \frac{\psi_{\ell j}(r) \psi_{\ell j}(r')}{k^2 + \kappa_j^2}. \quad (12)$$

The $i\epsilon$ prescription has been chosen so that this Green's function is meromorphic in the upper half-plane, with simple poles at the imaginary momenta $k = i\kappa_j$ corresponding to bound states. Thus we have

$$\begin{aligned} \epsilon(r) = & \sum_\ell N_\ell \int_{-\infty}^\infty \frac{dk}{2\pi i} \omega \left[1 + \frac{1}{4\omega^2} D_r \right] k G_\ell(r, r, k) \\ & + \sum_\ell N_\ell \sum_j \omega_j \left[1 + \frac{1}{4\omega_j^2} D_r \right] \psi_{\ell j}(r)^2 - \epsilon^{(0)}(r) + \epsilon_{\text{CT}}(r), \end{aligned} \quad (13)$$

where we have made use of the fact that for real k , the imaginary part of the Green's function at $r = r'$ is an odd function of k , while the real part is even. We would like to use eq. (13) to compute $\epsilon(r)$ as a contour integral in the upper half-plane. First we must eliminate the contribution from the semi-circular contour at large $|k|$ with $\text{Im}(k) \geq 0$. Using the techniques of Refs. [18] and [19] we see that subtracting sufficiently many terms in the

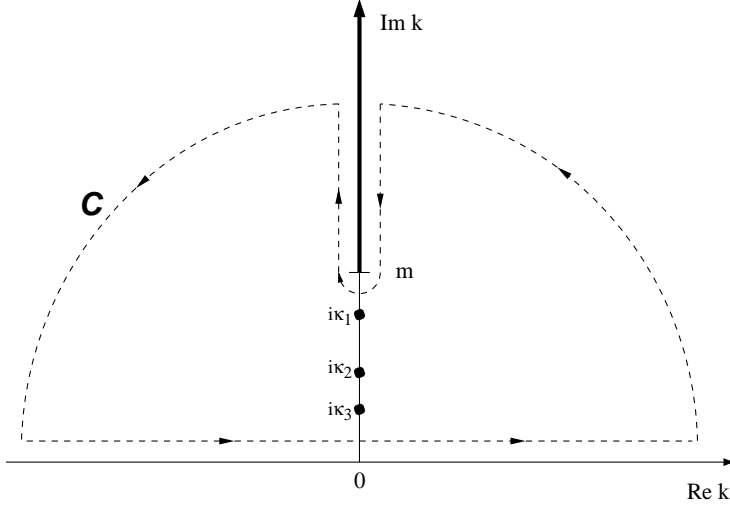


Figure 1: Contour for k integration.

Born series from the Green's function yields a convergent integral. We then add back exactly what we subtracted in the form of Feynman diagrams. We define

$$\begin{aligned}
 [\rho_\ell(k, r)]_N &\equiv [\rho_\ell(k, r) - \rho_\ell^{(0)}(k, r) - \rho_\ell^{(1)}(k, r) \dots - \rho_\ell^{(N)}(k, r)] \\
 &= \frac{k}{i} [G_\ell(r, r, k) - G_\ell^{(0)}(r, r, k) - G_\ell^{(1)}(r, r, k) - \dots - G_\ell^{(N)}(r, r, k)] \quad (14)
 \end{aligned}$$

where the superscript (j) indicates the term of order j in the Born expansion. Subtracting the free Green's function $G_\ell^{(0)}(r, r, k)$ corresponds to subtracting $\epsilon^{(0)}(r)$ above. We substitute $[\rho_\ell(k, r)]_N$ for $kG_\ell(r, r, k)/i$ in eq. (13) and add back in the Feynman diagrams corresponding to the subtractions in eq. (14), which we compute below. As a result, we obtain a finite expression amenable to contour integration. Furthermore, we have precisely identified the potentially divergent pieces with Feynman diagrams, which we can regularize and renormalize using standard methods. When combined with the contribution from the counterterms $\epsilon_{\text{CT}}(r)$ they yield finite contributions to the energy density (for smooth backgrounds).

We now have to specify the contour along which to compute the integral

$$\oint_C \frac{dk}{2\pi} \sqrt{k^2 + m^2} \left[1 + \frac{1}{4(k^2 + m^2)} D_r \right] [\rho_\ell(k, r)]_N. \quad (15)$$

The integrand has a branch cut along the imaginary axis $k \in [im, +i\infty]$ and simple poles at the bound state momenta $k = i\kappa_j$. We deform the integral around the cut as shown in Fig. 1, picking up the residues, which cancel the bound state contributions in eq. (13) [20]. Note that the Born terms do not introduce any poles. Hence we are left with the discontinuity along the cut,

$$\epsilon(r) = - \sum_\ell N_\ell \int_m^\infty \frac{dt}{\pi} \sqrt{t^2 - m^2} \left[1 - \frac{1}{4(t^2 - m^2)} D_r \right] [\rho_\ell(it, r)]_N + \sum_{i=1}^N \epsilon_{\text{FD}}^{(i)}(r) + \epsilon_{\text{CT}}(r)$$

$$\equiv \bar{\epsilon}(r) + \sum_{i=1}^N \epsilon_{\text{FD}}^{(i)}(r) + \epsilon_{\text{CT}}(r). \quad (16)$$

Here $\epsilon_{\text{FD}}^{(i)}(r)$ is the Feynman diagram contribution at order i in the background field. As emphasized in the Introduction, the representation of $\epsilon(r)$ as an integral along the imaginary axis is only useful if it can be computed efficiently. In the following subsections we show how to do so.

2.2 Computational Techniques

In this subsection we concentrate on $\bar{\epsilon}(r)$, the continuum integral in eq. (16). We develop a representation of the partial wave Green's function, $G_\ell(r, r', k)$ and its Born series, eq. (14), that can be computed efficiently for imaginary k . By working with pure imaginary momenta we avoid functions that would oscillate at large $|k|$. We will make extensive use of the analytic properties of scattering data [21].

We begin by introducing solutions to eq. (5) that obey a variety of different boundary conditions. First we define the free Jost solution

$$w_\ell(kr) = (-1)^\nu \sqrt{\frac{\pi}{2}kr} [J_\nu(kr) + iY_\nu(kr)], \quad (17)$$

where $\nu = \ell - 1 + \frac{n}{2}$. The radial function $w_\ell(kr)$ is a solution to eq. (5) with $\sigma \equiv 0$ describing an outgoing spherical wave. Then we define

- The *Jost solution*, $f_\ell(k, r)$. It behaves like an outgoing wave at $r \rightarrow \infty$, with

$$\lim_{r \rightarrow \infty} \frac{f_\ell(k, r)}{w_\ell(kr)} = 1. \quad (18)$$

- The *Jost function*, $F_\ell(k)$. It is obtained as the ratio of the interacting and free Jost solutions at $r = 0$,

$$F_\ell(k) = \lim_{r \rightarrow 0} \frac{f_\ell(k, r)}{w_\ell(kr)}. \quad (19)$$

- The *regular solution*, $\phi_\ell(k, r)$. It is defined by a k -independent boundary condition at the origin,

$$\lim_{r \rightarrow 0} \frac{\Gamma(\nu + 1)}{\sqrt{\pi}} \left(\frac{r}{2}\right)^{-(\nu + \frac{1}{2})} \phi_\ell(k, r) = 1. \quad (20)$$

- The *physical scattering solution*, $\psi_\ell(k, r)$. It is also regular at the origin (and thus proportional to $\phi_\ell(k, r)$), but differently normalized³

$$\psi_\ell(k, r) = \frac{k^{\nu + \frac{1}{2}}}{F_\ell(k)} \phi_\ell(k, r). \quad (21)$$

³Whenever a fractional power of k appears, we define it to be the limit as k approaches the real axis from above.

The reason for distinguishing two regular solutions is that ϕ_ℓ has a simple boundary condition at $r = 0$, while ψ_ℓ has a physical boundary condition at $r \rightarrow \infty$, corresponding to incoming and outgoing spherical waves. With these definitions, the Green's function has a simple representation

$$G_\ell(r, r', k) = \frac{\phi_\ell(k, r_<)f_\ell(k, r_>)}{F_\ell(k)}(-k)^{\nu-\frac{1}{2}}, \quad (22)$$

where $r_>$ ($r_<$) denotes the larger (smaller) of the two arguments r and r' . The poles of G occur at the zeros of the Jost function, which are the imaginary bound state momenta. Note that these are the only poles of eq. (12) in the upper half-plane, and since the two functions in eq. (12) and eq. (22) obey the same inhomogeneous differential equation they are indeed identical.

The representation of $G_\ell(r, r, k)$ in eq. (22) is not yet suitable for numerical computation on the imaginary axis. Although G_ℓ is analytic in the upper half-plane, f_ℓ and ϕ_ℓ contain pieces that oscillate for real k and exponentially increase or decrease respectively when k has an imaginary part. We are actually only interested in the case $r = r'$, in which case the product $f_\ell\phi_\ell$ is well-behaved. But because of the exponential behavior of the two factors, the product cannot be computed accurately by simply multiplying the individual functions obtained from numerical integration of the respective differential equations. To proceed, we factor out the dangerous exponential components with the following *ansatz*,⁴

$$f_\ell(k, r) \equiv w_\ell(kr)g_\ell(k, r)$$

and

$$\phi_\ell(k, r) \equiv \frac{(-k)^{-\nu+\frac{1}{2}} h_\ell(k, r)}{2\nu w_\ell(kr)}, \quad (23)$$

where w_ℓ is the free Jost solution introduced above. With these definitions,

$$G_\ell(r, r, k) = \frac{h_\ell(k, r)g_\ell(k, r)}{2\nu g_\ell(k, 0)}. \quad (24)$$

As we shall show, both $g_\ell(k, r)$ and $h_\ell(k, r)$ are well-behaved on the imaginary axis. Note that the definition of h_ℓ does *not* just remove the free part.⁵ Instead, it enforces the cancellation of w_ℓ in the Green's function. The factors in eq. (23) were chosen to provide a simple boundary condition on $h_\ell(k, r)$ at $r = 0$. After analytically continuing to $k = it$, $g_\ell(it, r)$ obeys

$$g_\ell''(it, r) = 2t\xi_\ell(tr)g_\ell'(it, r) + \sigma(r)g_\ell(it, r) \quad (25)$$

with the boundary conditions

$$\lim_{r \rightarrow \infty} g_\ell(it, r) = 1 \quad \text{and} \quad \lim_{r \rightarrow \infty} g_\ell'(it, r) = 0, \quad (26)$$

⁴For $n = 1$ and $n = 2$, the case of $\ell = 0$ is somewhat different. We will explore the former in Section 3 and the latter in Section 4.

⁵Removing the free part would correspond to an *ansatz* like $\phi_\ell \sim w_\ell h_\ell$ as in computations of functional determinants with Euclidean Green's functions [22].

where a prime indicates a derivative with respect to the radial coordinate r . Using these boundary conditions, we integrate this differential equation numerically for $g_\ell(it, r)$, starting at $r = \infty$ and proceeding to $r = 0$. Similarly, $h_\ell(it, r)$ obeys

$$h_\ell''(it, r) = -2t\xi_\ell(tr)h_\ell'(it, r) + \left[\sigma(r) - 2t^2 \frac{d\xi_\ell(\tau)}{d\tau} \Big|_{\tau=tr} \right] h_\ell(it, r) \quad (27)$$

with the boundary conditions

$$h_\ell(it, 0) = 0 \quad \text{and} \quad h_\ell'(it, 0) = 1 \quad (28)$$

and we integrate numerically from $r = 0$ to $r = \infty$. For real τ ,

$$\xi_\ell(\tau) \equiv -\frac{d}{d\tau} \ln [w_\ell(i\tau)] \quad (29)$$

is real with $\lim_{\tau \rightarrow \infty} \xi_\ell(\tau) = 1$, so the two functions $h_\ell(it, r)$ and $g_\ell(it, r)$ are manifestly real. They are also holomorphic in the upper k -plane and, most importantly, they are bounded according to

$$\begin{aligned} |g_\ell(k, r)| &\leq \text{const} \\ |h_\ell(k, r)| &\leq \text{const} \frac{2\nu r}{1 + |k|r} \end{aligned} \quad (30)$$

so that neither g_ℓ nor h_ℓ grows exponentially during the numerical integration. Thus the representation of the partial wave Green's function in terms of g_ℓ and h_ℓ is smooth and numerically tractable on the positive imaginary axis. We have avoided oscillating functions or exponentially growing functions that eventually would cancel against exponentially decaying functions.

Finally, the computation of the Born series, eq. (14), is also straightforward in this formalism. We expand the solutions to the differential equations eq. (25) and eq. (27) about the free solutions,

$$\begin{aligned} g_\ell(it, r) &= 1 + g_\ell^{(1)}(it, r) + g_\ell^{(2)}(it, r) + \dots \\ h_\ell(it, r) &= 2\nu r I_\nu(tr) K_\nu(tr) + h_\ell^{(1)}(it, r) + h_\ell^{(2)}(it, r) + \dots, \end{aligned} \quad (31)$$

where the superscript labels the order of the background potential σ . The higher order components obey inhomogeneous linear differential equations with the boundary conditions

$$\begin{aligned} \lim_{r \rightarrow \infty} g_\ell^{(j)}(it, r) &= 0 \quad \text{and} \quad \lim_{r \rightarrow \infty} g_\ell^{(j)'}(it, r) = 0, \\ h_\ell^{(j)}(it, 0) &= 0 \quad \text{and} \quad h_\ell^{(j)'}(it, 0) = 0. \end{aligned} \quad (32)$$

In these equations σ is the source term for $g^{(1)}$, $\sigma g^{(1)}$ is the source term for $g^{(2)}$, and so on. We then obtain the Born series for the local spectral density by substituting these solutions in the expansion of eq. (24) with respect to the order of the background potential. Thus

we have developed a computationally robust representation for the Born subtracted local spectral density,

$$[\rho_\ell(it, r)]_N = \left[t \frac{h_\ell(it, r) g_\ell(it, r)}{2\nu g_\ell(it, 0)} \right]_N. \quad (33)$$

2.3 Feynman Diagram Contribution

In this subsection we develop methods to compute the contribution from the Feynman diagrams and counterterms, $\sum_{i=0}^N \epsilon_{\text{FD}}^{(i)}(r) + \epsilon_{\text{CT}}(r)$, in eq. (16). To one-loop order, the Feynman diagrams of interest are generated by the expansion of

$$\langle 0 | \hat{T}_{00}(x) | 0 \rangle \sim \frac{i}{2} \text{Tr} \left[\hat{T}_x \left(-\partial^2 - m^2 - \sigma \right)^{-1} \right] \quad (34)$$

to order N in the background σ . Here \hat{T}_x is the coordinate space operator corresponding to the insertion of the energy density defined by eq. (1) at the spacetime point x , and the trace includes space-time integration. Since we are doing ordinary perturbation theory, we take the matrix elements with respect to the trivial vacuum, which is annihilated by the plane wave annihilation operators. The energy density operator has pieces of order σ^0 and σ^1 ,

$$\hat{T}_{00} = \frac{1}{2} \left[\dot{\phi}^2 + (\vec{\nabla}\phi)^2 + m^2\phi^2 + \sigma\phi^2 \right] = \frac{1}{2} \int d^d y \phi(y) \left(\hat{T}_x^{(0)} + \hat{T}_x^{(1)} \right) \phi(y) \quad (35)$$

where $d = n + 1$ is the number of space-time dimensions. We have separated the different orders in the external background field,

$$\begin{aligned} \hat{T}_x^{(0)} &= \left[\overleftarrow{\partial}_t \delta(x - \hat{y}) \overrightarrow{\partial}_t + \overleftarrow{\nabla} \delta(x - \hat{y}) \overrightarrow{\nabla} + m^2 \delta(x - \hat{y}) \right] \\ \hat{T}_x^{(1)} &= \sigma(x) \delta(x - \hat{y}). \end{aligned} \quad (36)$$

The δ -functions are understood as d -dimensional. The arrows denote the direction in which the derivatives act when substituting this representation into the functional trace in eq. (34) and \hat{y} is the coordinate space position operator, with $\hat{y}|\xi\rangle = \xi|\xi\rangle$. However, it is more convenient to perform the computation in momentum space. The relevant matrix elements are

$$\begin{aligned} \langle k' | \hat{T}_x^{(0)} | k \rangle &= e^{i(k' - k)x} \left[k'^0 k^0 + \vec{k}' \cdot \vec{k} + m^2 \right] \\ \langle k' | \hat{T}_x^{(1)} | k \rangle &= \sigma(x) e^{i(k' - k)x}. \end{aligned} \quad (37)$$

Here we will explicitly consider the contributions to $\langle \hat{T}_{00} \rangle$ that are linear in σ because these are the only contributions required in the examples studied in Sections 3 and 4. The first piece comes directly from $\hat{T}_x^{(1)}$ as shown in the left panel of Fig. 2,

$$\frac{i}{2} \text{Tr} \left(\frac{1}{-\partial^2 - m^2} \hat{T}_x^{(1)} \right) = \frac{i}{2} \sigma(x) \int \frac{d^d k}{(2\pi)^d} \frac{1}{k^2 - m^2}. \quad (38)$$



Figure 2: First order Feynman diagrams contributing to the energy density $\langle \hat{T}_{00}(x) \rangle$. The solid circle represents the ϕ loop and the operator insertions from eq. (36) are denoted by $\hat{T}_x^{(0,1)}$. In the right panel, σ is the local insertion of the background field from expanding the propagator, cf. eq. (39).

This local contribution is ultraviolet divergent for $d \geq 2$. It is canceled identically by the counterterm in the no-tadpole renormalization scheme, since the right-hand side of eq. (38) equals minus the counterterm Lagrangian evaluated for the background field σ . For further discussion of this renormalization condition and its consequences, see Ref. [15]. The second contribution at order σ originates from $\hat{T}_x^{(0)}$ and the first-order expansion of the propagator as shown in Fig. 2,

$$\frac{i}{2} \text{Tr} \left(\frac{1}{-\partial^2 - m^2} \hat{T}_x^{(0)} \frac{1}{-\partial^2 - m^2} \sigma \right). \quad (39)$$

For this diagram we find

$$\begin{aligned} & \frac{i}{2} \int \frac{d^d k}{(2\pi)^d} \int \frac{d^d k'}{(2\pi)^d} \frac{1}{k^2 - m^2} e^{i(k'-k)x} (\tilde{k} \cdot k' + m^2) \frac{1}{k'^2 - m^2} \tilde{\sigma}(k - k') \\ &= \frac{i}{2} \int \frac{d^d q}{(2\pi)^d} \tilde{\sigma}(q) e^{-iqx} \int_0^1 d\zeta \int \frac{d^d l}{(2\pi)^d} \frac{\tilde{l} \cdot l + m^2 - \zeta(1-\zeta)\tilde{q} \cdot q}{[l^2 - m^2 + \zeta(1-\zeta)q^2]^2}, \end{aligned} \quad (40)$$

where $\tilde{\sigma}(q) = 2\pi\delta(q^0)\tilde{\sigma}(\vec{q})$ is the Fourier transform of the (time independent) background field. We have defined $\tilde{p} = (p^0, -\vec{p})$ for the Lorentz-vector $p = (p^0, \vec{p})$. The leading ultraviolet divergences cancel in eq. (40) between the temporal and spatial components. We thus obtain the expression for the Feynman diagram and counterterm contribution through first order in σ ,

$$\begin{aligned} \epsilon_{\text{FD}}^{(1)}(r) + \epsilon_{\text{CT}}(r) &= \frac{2\pi^{\frac{n}{2}} r^{n-1}}{\Gamma(\frac{n}{2})} \frac{i}{2} \text{Tr} \left(\frac{1}{-\partial^2 - m^2} \hat{T}_x^{(0)} \frac{1}{-\partial^2 - m^2} \sigma \right) \\ &= \frac{2\pi^{\frac{n}{2}} r^{n-1}}{\Gamma(\frac{n}{2})} \frac{\Gamma(2 - \frac{d}{2})}{(4\pi)^{d/2}} \int \frac{d^n q}{(2\pi)^n} \tilde{\sigma}(\vec{q}) e^{i\vec{q} \cdot \vec{x}} \int_0^1 d\zeta \frac{\zeta(1-\zeta)\vec{q}^2}{[m^2 + \zeta(1-\zeta)\vec{q}^2]^{2-d/2}} \end{aligned} \quad (41)$$

We note that this piece does not contribute to the total energy because it vanishes when integrated over space. The extension to higher order Feynman diagrams in σ is straightforward. For example, the contribution $\mathcal{O}(\sigma^2)$ is obtained from the two terms

$$\frac{i}{2} \text{Tr} \left(\hat{T}_x^{(1)} \frac{1}{\partial^2 + m^2} \sigma \frac{1}{\partial^2 + m^2} \right) - \frac{i}{4} \text{Tr} \left(\hat{T}_x^{(0)} \frac{1}{\partial^2 + m^2} \sigma \frac{1}{\partial^2 + m^2} \sigma \frac{1}{\partial^2 + m^2} \right). \quad (42)$$

We use the matrix elements, eq. (37), to write this in terms of ordinary loop integrals

$$\frac{i}{2} \sigma(x) \int \frac{d^d q}{(2\pi)^d} \tilde{\sigma}(q) e^{iqx} \int_0^1 d\zeta \frac{d^d l}{(2\pi)^d} \frac{1}{[l^2 - m^2 + \zeta(1-\zeta)q^2]^2}$$

$$\begin{aligned}
& + \frac{i}{2} \int \frac{d^d q}{(2\pi)^d} \int \frac{d^d p}{(2\pi)^d} \tilde{\sigma}(q-p) \tilde{\sigma}(p) e^{-iqx} \\
& \times \int_0^1 d\zeta \int_0^{1-\zeta} d\eta \int \frac{d^d l}{(2\pi)^d} \frac{\tilde{l} \cdot l + [\zeta \tilde{q} + \eta \tilde{p}] \cdot [(1-\zeta)q - \eta p]}{[l^2 - m^2 + \zeta(1-\zeta)q^2 + \eta(1-\eta)p^2]^3}.
\end{aligned} \tag{43}$$

As a consequence of eq. (37), the term involving $\hat{T}_x^{(1)}$ will always carry an explicit factor of $\sigma(x)$.

2.4 Total Energy

We can obtain the total energy simply by integrating the energy density in eq. (16),

$$E[\sigma] = \int_0^\infty \epsilon(r) dr. \tag{44}$$

Since both the t integral and the sum over channels in eq. (16) are absolutely convergent, we can interchange the order of integration and obtain

$$E[\sigma] = - \sum_\ell N_\ell \int_m^\infty \frac{dt}{\pi} \sqrt{t^2 - m^2} \int_0^\infty dr [\rho_\ell(it, r)]_N + \sum_{i=1}^N E_{\text{FD}}^{(i)} + E_{\text{CT}}, \tag{45}$$

where the total derivative term has integrated to zero. As explained in the previous subsection, we have to subtract a sufficient number of Born approximations to the local spectral density $\rho_\ell(it, r)$ to render the t integral convergent. These subtractions are then added back in as the contribution to the total energy from the Feynman diagrams

$$\sum_{i=1}^N E_{\text{FD}}^{(i)} = \sum_{i=1}^N \int_0^\infty dr \epsilon_{\text{FD}}^{(i)}(r), \tag{46}$$

which we then combine with the contribution from the counterterms

$$E_{\text{CT}} = \int_0^\infty dr \epsilon_{\text{CT}}(r) \tag{47}$$

to obtain a finite result. In practice, these terms can be more efficiently computed directly from the perturbation series of the total energy. For the first term in eq. (45), we employ the relation

$$2 \int_0^\infty dr [\rho_\ell(k, r)]_0 = \frac{2k}{i} \int_0^\infty dr [G_\ell(r, r, k) - G_\ell^{(0)}(r, r, k)] = i \frac{d}{dk} \ln F_\ell(k) \tag{48}$$

which we prove in Appendix A for all k in the upper half-plane, $\text{Im } k > 0$. Using eq. (48) on the imaginary axis $k = it$, we find in particular

$$2 \int_0^\infty dr [\rho(it, r)]_0 = \frac{d}{dt} \ln F_\ell(it) = \frac{d}{dt} \ln \lim_{r \rightarrow 0} \frac{f_\ell(it, r)}{w_\ell(itr)} = \frac{d}{dt} \ln g_\ell(it, 0). \tag{49}$$

Finally, we introduce the real function $\beta_\ell(t, r) = \ln g_\ell(it, r)$ and write

$$\begin{aligned} E[\sigma] &= -\sum_\ell N_\ell \int_m^\infty \frac{dt}{2\pi} \sqrt{t^2 - m^2} \frac{d}{dt} [\beta_\ell(t, 0)]_N + \sum_{i=1}^N E_{\text{FD}}^{(i)} + E_{\text{CT}} \\ &= \sum_\ell N_\ell \int_m^\infty \frac{dt}{2\pi} \frac{t}{\sqrt{t^2 - m^2}} [\beta_\ell(t, 0)]_N + \sum_{i=1}^N E_{\text{FD}}^{(i)} + E_{\text{CT}}, \end{aligned} \quad (50)$$

where β_ℓ is determined by the differential equation

$$-\beta_\ell''(t, r) - [\beta_\ell'(t, r)]^2 + 2t\xi_\ell(tr)\beta_\ell'(k, r) + \sigma(r) = 0 \quad (51)$$

with the boundary conditions $\lim_{r \rightarrow \infty} \beta(t, r) = \lim_{r \rightarrow \infty} \beta'(t, r) = 0$. To compute $[\beta_\ell(t, 0)]_N$, we must subtract the first N Born terms, which we compute by iterating the differential equation (51) according to the expansion of $\beta_\ell(t, r)$ in powers of the interaction σ .

The formulation (50) is well suited for numerical evaluation and we will use it exclusively to compute the total energy. To make contact with previous work [15], however, it is instructive to return to the real axis. We rotate the contour in eq. (50) to obtain an integral over the whole real axis, picking up the discrete contributions from the bound state poles. When k approaches the real axis from above, we have

$$i \frac{d}{dk} \ln F_\ell(k) = i \frac{d}{dk} \ln |F_\ell(k)| + \frac{d\delta_\ell(k)}{dk} \quad (52)$$

where $\delta_\ell(k)$ is the phase shift. The first term on the right-hand side is odd in k and does not contribute to the integral. Thus we have

$$E[\sigma] = \sum_\ell N_\ell \left[\int_0^\infty \frac{dk}{2\pi} \sqrt{k^2 + m^2} \frac{d}{dk} [\delta_\ell(k)]_N + \frac{1}{2} \sum_j \omega_j \right] + \sum_{i=1}^N E_{\text{FD}}^{(i)} + E_{\text{CT}} \quad (53)$$

which was used in [15]. To understand the physical motivation for eq. (53), we introduce the difference between the free and interacting density of states,

$$\frac{2k}{\pi} \text{Im} \int_0^\infty \left(G_\ell(r, r, k + i\epsilon) - G_\ell^{(0)}(r, r, k + i\epsilon) \right) dr = \rho_\ell(k) - \rho_\ell^{(0)}(k), \quad (54)$$

which from eq. (48) and eq. (52) is related to the phase shift by

$$\rho_\ell(k) - \rho_\ell^{(0)}(k) = \frac{1}{\pi} \frac{d\delta_\ell}{dk}. \quad (55)$$

Thus we can write the energy as

$$E[\sigma] = \sum_\ell N_\ell \left[\int_0^\infty \frac{dk}{2\pi} \sqrt{k^2 + m^2} [\rho_\ell(k)]_N + \frac{1}{2} \sum_j \omega_j \right] + \sum_{i=1}^N E_{\text{FD}}^{(i)} + E_{\text{CT}}, \quad (56)$$

and see that it is simply the sum of the zero-point energies $\frac{1}{2}\omega$, including both discrete contributions from the bound states and an integral over the continuum, weighted by the density of states.

We can also see this relation directly by integrating eq. (9) over r , with N Born terms subtracted and added back in as diagrams,

$$E[\sigma] = \sum_{\ell} N_{\ell} \left[\int_{0+i\epsilon}^{\infty+i\epsilon} \frac{dk}{\pi} \sqrt{k^2 + m^2} \int_0^{\infty} dr [\psi_{\ell}^*(k, r) \psi_{\ell}(k, r)]_N + \sum_j \frac{\omega_j}{2} \right] + \sum_{i=1}^N E_{\text{FD}}^{(i)} + E_{\text{CT}}, \quad (57)$$

where the total derivative term has integrated to zero and the bound state wavefunctions have integrated to unity. We can then use eq. (A.14) to see that eq. (57) is equivalent to eq. (56). While this relation is useful for building an intuitive understanding of the expressions for the total energy and the energy density, eq. (57) is of no practical use in numerical calculations; it only converges because eq. (54) has introduced the standard $i\epsilon$ prescription to control the oscillations of the wavefunctions at spatial infinity. Any direct numerical calculation using eq. (57) will be hopelessly obscured by these oscillations.

3. Examples in One Space Dimension

To illustrate our method, we apply it first to simple Casimir problems in one space dimension. There are only two channels (symmetric and antisymmetric) in this case. The boundary condition in the symmetric channel, $\frac{d\phi}{dx}|_{x=0} = 0$, requires slight modifications of the formalism developed so far. We study two examples: a background field consisting of δ -functions, which allows us to make contact with treatments already in the literature [3, 4], and a Gaussian background, to demonstrate the efficient use of our methods for numerical computation.

3.1 Green's Function

In one spatial dimension, the S-matrix for a symmetric potential is diagonalized in a basis of symmetric and antisymmetric wavefunctions. In the antisymmetric channel, we can proceed with the general techniques described in Section 2. From eqs. (25) and (27) we compute $g(it, x)$ and $h_{-}(it, x)$ with $\xi = 1$. Note that $g(it, x)$ is the same in both channels because the channels only differ by the boundary conditions at the origin, which do not affect g . At equal spatial arguments we have

$$G_{-}(x, x, it) = \frac{h_{-}(it, x)g(it, x)}{g(it, 0)}. \quad (58)$$

However, the boundary conditions in the symmetric channel,

$$\phi_{+}(0) = 1 \quad \text{and} \quad \phi'_{+}(0) = 0, \quad (59)$$

are not in the class defined by eq. (20). Constructing the Jost solution $f(k, x)$ with the boundary condition $\lim_{x \rightarrow \infty} f(k, x)e^{-ikx} = 1$ and working out the Wronskian for ϕ_{+} and f yields the Green's function in the symmetric channel

$$G_{+}(x, y, k) = -\frac{\phi_{+}(k, x_{<})f(k, x_{>})}{f'(k, 0)}, \quad (60)$$

where $f'(k, 0) = \partial_x f(k, x)|_{x=0}$. By symmetry we have $G_+(-x, -y, k) = G_+(x, y, k)$. We factor out the asymptotic behavior,

$$\phi_+(k, x) = e^{-ikx} h_+(k, x) \quad (61)$$

and obtain

$$-h_+''(it, x) - 2th_+'(it, x) + \sigma(x)h_+(it, x) = 0. \quad (62)$$

which is the same differential equation obeyed by $h_-(it, x)$. The boundary conditions in eq. (59) then become

$$h_+(it, 0) = 1 \quad \text{and} \quad h_+'(it, 0) = -t. \quad (63)$$

With this solution, we can now construct the Green's function in the symmetric channel. To compute densities it again suffices to consider $x = y$, where we have

$$G_+(x, x, it) = \frac{g(it, x)h_+(it, x)}{tg(it, 0) - g'(it, 0)} \quad (64)$$

and the complete Green's function is the sum $G = G_+ + G_-$, giving

$$\rho(it, x) = t \frac{g(it, x)h_-(it, x)}{g(it, 0)} + \frac{g(it, x)h_+(it, x)}{g(it, 0) - g'(it, 0)/t}. \quad (65)$$

The Born series is then obtained by iteration of the differential equations (25), (27), and (62).

3.2 Total Energy

The contribution of the symmetric channel to the total energy cannot be cast in the general form of eq. (50) because, as for the Green's function, the boundary condition for the corresponding wavefunction is not of the type of eq. (20). Since the derivative of ϕ_+ vanishes at $x = 0$, the Jost function becomes

$$F_+(k) = \lim_{x \rightarrow 0} \frac{f'(k, x)}{ik} = g(k, 0) + \frac{g'(k, 0)}{ik} \quad (66)$$

which is normalized so that $F_+(k) = 1$ when $\sigma \equiv 0$. Otherwise, the same analyticity arguments apply as in channels whose wavefunctions vanish at $r = 0$. In particular, the k integration contour can be closed around the discontinuity along the positive imaginary axis. We obtain

$$E[\sigma] = \int_m^\infty \frac{dt}{2\pi} \frac{t}{\sqrt{t^2 - m^2}} \left[\ln g(it, 0) + \ln \left(g(it, 0) - \frac{1}{t} g'(it, 0) \right) \right]_1 + E_{\text{FD}}^{(1)} + E_{\text{CT}}, \quad (67)$$

where as before the subscript indicates that the first Born term has been removed from the expression in brackets. One subtraction suffices in one dimension. By our no-tadpole

renormalization condition, the counterterm cancels the tadpole diagram identically, so that $E_{\text{FD}}^{(1)} + E_{\text{CT}} \equiv 0$.

3.3 Delta–Function Background

We first consider the case of two δ -functions separated by a distance $2a$,

$$\sigma_\delta(x) = \lambda [\delta(x+a) + \delta(x-a)] . \quad (68)$$

At each δ -function, the derivative of the field ϕ jumps by $\lambda\phi$. For modes with $k \ll \lambda$, the wavefunction $\psi(k, x)$ vanishes at $\pm a$, so that the limit $\lambda \rightarrow \infty$ gives a Dirichlet boundary condition at $\pm a$. Since the counterterms are local functionals of the background field, they are identically zero in regions where the background fields vanish. Hence in a renormalizable theory, local observables such as the energy density cannot have ultraviolet divergences in these regions, as we will see explicitly below.

By integration of the respective differential equations we obtain

$$\begin{aligned} g(it, x) &= \begin{cases} 1 & |x| > a \\ 1 + \frac{\lambda}{2t} [1 - e^{2t(x-a)}] & 0 \leq |x| < a \end{cases} \\ h_+(it, x) &= \frac{1}{2} \begin{cases} 1 + e^{-2tx} + \frac{\lambda}{2t} [1 + e^{-2ta} - e^{-2tx} - e^{-2t(x-a)}] & |x| > a \\ 1 + e^{-2tx} & 0 \leq |x| < a \end{cases} \\ h_-(it, x) &= \frac{1}{2t} \begin{cases} 1 - e^{-2tx} + \frac{\lambda}{2t} [1 - e^{-2ta} + e^{-2tx} - e^{-2t(x-a)}] & |x| > a \\ 1 - e^{-2tx} & 0 \leq |x| < a \end{cases} \end{aligned} \quad (69)$$

It is clear that g , h_+ , and h_- are all well-behaved for $t > 0$. We substitute $g(it, 0)$ and its derivative into eq. (67) and find the total energy

$$E_2(a, \lambda) = \int_m^\infty \frac{dt}{2\pi} \frac{1}{\sqrt{t^2 - m^2}} \left\{ t \ln \left[1 + \frac{\lambda}{t} + \frac{\lambda^2}{4t^2} (1 - e^{-4ta}) \right] - \lambda \right\} . \quad (70)$$

The last term in curly brackets is the $N = 1$ Born subtraction. Carrying out a similar calculation for a single δ -function, we obtain

$$E_1(\lambda) = \int_m^\infty \frac{dt}{2\pi} \frac{t \ln \left[1 + \frac{\lambda}{2t} \right] - \frac{\lambda}{2}}{\sqrt{t^2 - m^2}} \quad (71)$$

$$= \frac{\lambda - m\pi}{4\pi} + \frac{m}{2\pi} \begin{cases} \sqrt{1 - \frac{\lambda^2}{4m^2}} \arccos \frac{\lambda}{2m} & \lambda \leq 2m \\ \sqrt{\frac{\lambda^2}{4m^2} - 1} \ln \left(\frac{\lambda}{2m} - \sqrt{\frac{\lambda^2}{4m^2} - 1} \right) & \lambda > 2m . \end{cases} \quad (72)$$

From eq. (72) we can verify that E_1 and E_2 obey the consistency conditions $\lim_{a \rightarrow \infty} E_2(a, \lambda) = 2E_1(\lambda)$ and $\lim_{a \rightarrow 0} E_2(a, \lambda) = E_1(2\lambda)$.

We observe that in the limit of large λ the total energy associated with a single δ -function approaches minus infinity as $-\lambda \ln \lambda$, which cannot be canceled by any available counterterm. Thus in this limit the energy is infinite. *In this sense the Dirichlet-Casimir problem is not well defined in the context of renormalizable quantum field theory.* However, we can compute the force between two δ -functions for finite λ and subsequently take the $\lambda \rightarrow \infty$ limit,

$$K(a) = - \lim_{\lambda \rightarrow \infty} \frac{\partial E_2(a, \lambda)}{\partial(2a)} = - \int_m^\infty \frac{dt}{\pi} \frac{t^2}{\sqrt{t^2 - m^2} (e^{4ta} - 1)}. \quad (73)$$

which is equal to the result found using boundary conditions [3]. The massless limit does not exist for the vacuum polarization energy in eq. (72), even for finite λ . This is to be expected since massless scalar field theories are infrared divergent in $1 + 1$ dimensions. However, it exists for the force, yielding the well-known result

$$\lim_{m \rightarrow 0} K(a) = -\frac{\pi}{96a^2}. \quad (74)$$

Next we turn to the energy density. In this Section, we consider the energy density $\epsilon(x) = \langle T_{00} \rangle$ without factoring out the surface area factor as we did in the previous Section (which would just give a factor of 2 here). The resulting energy density $\epsilon(x)$ is normalized such that $\int_{-\infty}^\infty \epsilon(x) dx$ gives the total energy. It is convenient to decompose the energy density into $\bar{\epsilon}(x)$, the integral over the subtracted local spectral density, and $\epsilon_{\text{FD}}^{(1)}(x) + \epsilon_{\text{CT}}(x)$, the contribution of the Feynman diagram plus counterterms.

First we study $\bar{\epsilon}(x)$. From the radial functions in eq. (69), we find the local spectral density as a function of x and $k = it$,

$$[\rho(it, x)]_0 = \frac{\lambda}{\lambda^2 - (2t + \lambda)^2 e^{4ta}} \begin{cases} [2t - \lambda + (2t + \lambda)e^{4ta}] e^{2t(a-|x|)} & |x| > a \\ 2 [(2t + \lambda)e^{2ta} \cosh(2tx) - \lambda] & 0 \leq |x| < a, \end{cases} \quad (75)$$

where only the free local spectral density has been subtracted. For $|x| \neq a$ the local spectral density decays exponentially as t increases, so it yields a finite energy density without any subtractions, as we expected since the counterterm vanishes away from $x = \pm a$.

To prepare for more general problems involving smooth potentials, where the energy will diverge at all x , we carry out the full Born subtraction procedure even though in this case the Born subtraction and the diagram contribution are both finite and equal for all $|x| \neq a$, and so their contributions cancel. We will thus obtain the energy density everywhere including the points $x = \pm a$. The first Born approximation is given by

$$\rho^{(1)}(it, x) = -\frac{\lambda}{2t} \begin{cases} e^{-2t(|x|-a)} + e^{-2t(|x|+a)}, & |x| > a \\ e^{2t(|x|-a)} + e^{-2t(|x|+a)}, & 0 \leq |x| < a \end{cases} \quad (76)$$

and we obtain

$$\bar{\epsilon}(x, a, \lambda) = \int_m^\infty \frac{dt}{\pi} \frac{\eta(it, x)}{\sqrt{t^2 - m^2}} \quad (77)$$

where

$$\begin{aligned} \eta(it, x) &= \frac{\lambda^2 2t - \lambda + (2t + \lambda)e^{4ta}}{2 \lambda^2 - (2t + \lambda)^2 e^{4ta}} \delta(|x| - a) \\ &+ \frac{m^2 \lambda^2 / t}{(2t + \lambda)^2 e^{4ta} - \lambda^2} \begin{cases} \frac{1}{2} [6t - \lambda e^{-4ta} + (2t + \lambda)e^{4ta}] e^{2t(a-|x|)} & |x| > a \\ \frac{2t}{m^2} (m^2 - t^2) + [(2t + \lambda)e^{2ta} - \lambda e^{-2ta}] \cosh(2tx) & 0 \leq |x| < a. \end{cases} \end{aligned} \quad (78)$$

For the Feynman diagram and the counterterm, we use eq. (41) and split off a δ -function contribution,

$$\begin{aligned} \epsilon_{\text{FD}}^{(1)}(x, a, \lambda) + \epsilon_{\text{CT}}(x, a, \lambda) &= \frac{\lambda}{2\pi} \delta(|x| - a) \\ &- \frac{\lambda}{\pi^2} \int_0^\infty dq \cos(qa) \cos(qx) \int_0^1 d\zeta \frac{m^2}{m^2 + \zeta(1-\zeta)q^2}. \end{aligned} \quad (79)$$

We recast the second term in a form which makes its identification with the first Born contribution, eq. (76), manifest,

$$\begin{aligned} \epsilon_{\text{FD}}^{(1)}(x, a, \lambda) + \epsilon_{\text{CT}}(x, a, \lambda) &= \frac{\lambda}{2\pi} \delta(|x| - a) - \frac{4m^2 \lambda}{\pi^2} \int_0^\infty dq \frac{\cos(qa) \cos(qx)}{q \sqrt{q^2 + 4m^2}} \sinh^{-1} \frac{q}{2m} \\ &= \frac{\lambda}{2\pi} \delta(|x| - a) - \frac{m^2 \lambda}{2\pi} \int_m^\infty \frac{dt}{t \sqrt{t^2 - m^2}} \left[e^{-2|x-a|t} + e^{-2|x+a|t} \right], \end{aligned} \quad (80)$$

which confirms that our Feynman diagram representation of the $\mathcal{O}(\lambda)$ contribution to $\epsilon(x, a, \lambda)$ agrees with the k integral representation for values of x where the counterterms vanish.

In Fig. 3 we display the energy density for two delta functions separated by $2a$, $\epsilon_2(x, a, \lambda)$ as functions of x . Note that there are δ -function contributions to $\epsilon_2(x, a, \lambda)$ at $x = \pm a$ not drawn in the figure. For reference we also show the sum of the energy densities for delta functions at $x = a$ and $x = -a$ separately, which we denote $\epsilon_1(x \mp a, \lambda)$. The difference between $\epsilon_2(x, a, \lambda)$ and the sum $\epsilon_1(x - a, \lambda) + \epsilon_1(x + a, \lambda)$ will result in a force between the two points.

As $\lambda \rightarrow \infty$, we expect to obtain the same energy density as if we had imposed the boundary conditions $\phi(-a) = \phi(a) = 0$ from the outset. No subtraction is necessary away from $x = \pm a$, so we can study the energy density in this region directly from $[\rho]_0$, given in eq. (75),

$$\lim_{\lambda \rightarrow \infty} \epsilon_2(x) = -\frac{1}{\pi} \int_m^\infty \frac{dt}{\sqrt{t^2 - m^2}} \frac{t^2 - m^2 + m^2 e^{2ta} \cosh(2tx)}{e^{4at} - 1} \quad \text{for } |x| < a. \quad (81)$$

To compare with Ref. [3], we separate the x -dependent part and transform the t integral into a sum over the poles of the function $e^{2ta}/(e^{4at} - 1) = 1/(2 \sinh 2ta)$ at $t = in\pi/2a$,

$$\lim_{\lambda \rightarrow \infty} \epsilon_2(x) = -\frac{1}{\pi} \int_m^\infty \frac{dt}{\sqrt{t^2 - m^2}} \frac{t^2 - m^2}{e^{4at} - 1} - \frac{m}{8a} - \frac{m^2}{4a} \sum_{n=1}^\infty \frac{\cos \left[\frac{n\pi}{a} (|x| - a) \right]}{\sqrt{\left(\frac{n\pi}{2a} \right)^2 + m^2}} \quad \text{for } |x| < a. \quad (82)$$

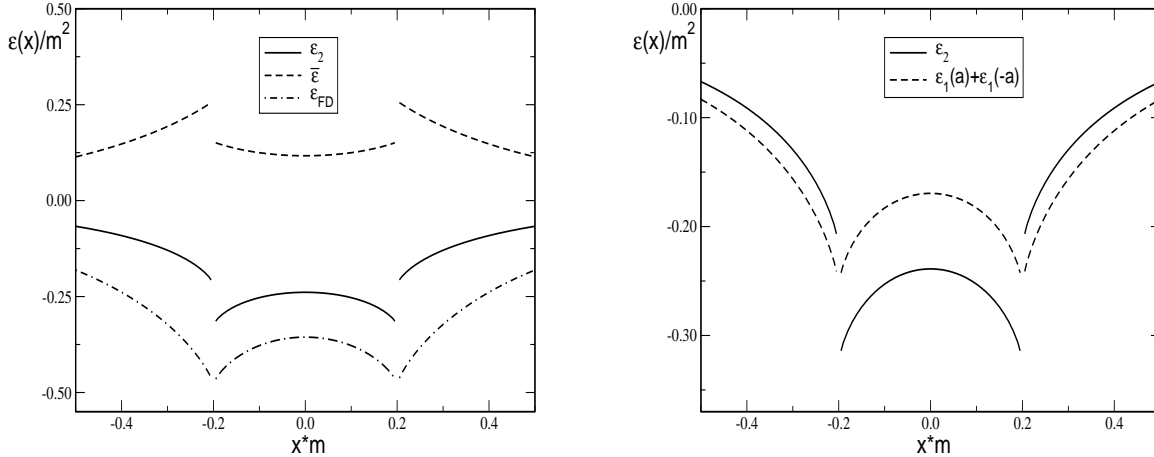


Figure 3: Left panel: The total energy density $\epsilon_2(x, a, \lambda)$ and the contributions $\bar{\epsilon}(x, a, \lambda)$ and $\epsilon_{\text{FD}}^{(1)}(x, a, \lambda)$, defined in eqs. (77) and (80). Note that the displayed energy densities are supplemented by δ -function contributions located at $x = a$ and $x = -a$. Right panel: The total density $\epsilon_2(x, a, \lambda)$ compared to the sum $\epsilon_1(x - a, \lambda) + \epsilon_1(x + a, \lambda)$ of the energy densities of two isolated δ -functions. The parameters are $\lambda = 3m$ and $a = 0.2/m$.

This expression agrees with the Dirichlet result given in Ref. [3].

This simple example allows us to study the nature of the divergence in the Dirichlet Casimir energy in the limit $\lambda \rightarrow \infty$. For any fixed x away from the δ -functions, the energy density reaches a finite limit as $\lambda \rightarrow \infty$, but the limit is approached nonuniformly. This can be seen clearly in Fig. 4, where we display the energy density for large couplings and compare it to the limiting function, eq. (81). The closer x approaches to a , the slower the energy density converges to its limiting form. Thus the energy density away from the source on the boundary remains finite and well defined in the boundary condition limit even though the total energy diverges.

3.4 Gaussian Background Field

In this subsection we demonstrate how to calculate the energy density associated with a Gaussian background using our method. This problem is a warmup for the next Section, where we will use a tall, narrow Gaussian background as an approximation to the δ -function in higher dimensions, where the energy of a delta function diverges even at finite coupling. We choose a Gaussian background that approximates the δ -function potential from the previous subsection,

$$\sigma_{\text{G}}(x) = \frac{A}{2} \left[e^{-\frac{(x-a)^2}{2w^2}} + e^{-\frac{(x+a)^2}{2w^2}} \right], \quad (83)$$

in the limit $w \rightarrow 0$ where A is chosen so that the area under the Gaussian is fixed to 2λ . We substitute this background field into the differential equations (25), (27) and (62) and obtain the wavefunctions g , h_- and h_+ numerically. As promised, these functions are well-behaved on the positive imaginary k axis. At large momenta t , we expect $h_-(it, x)$ to approach the free solution, which decays asymptotically as $(1 + e^{-t|x|})/2t$. This behavior can be seen

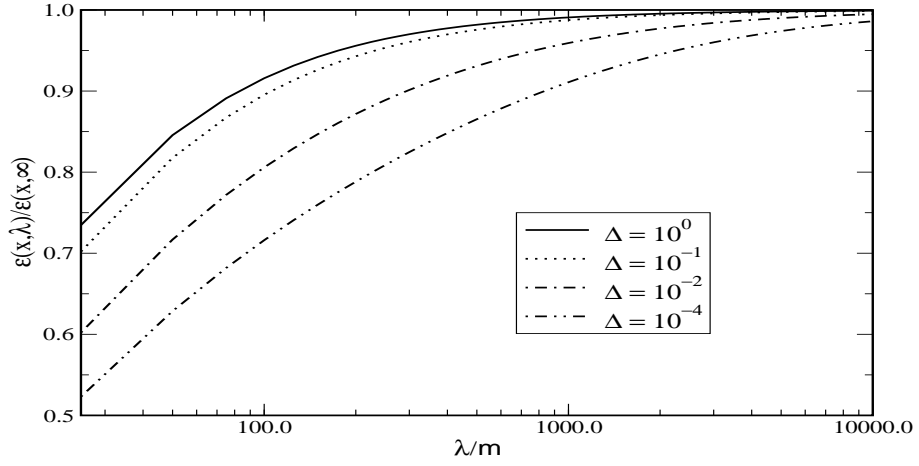


Figure 4: Ratio of the energy density for two δ -functions with finite λ to the energy density for $\lambda \rightarrow \infty$ with $a = 0.2/m$, plotted as a function of λ for several values of $\Delta = (a - x)/a$.

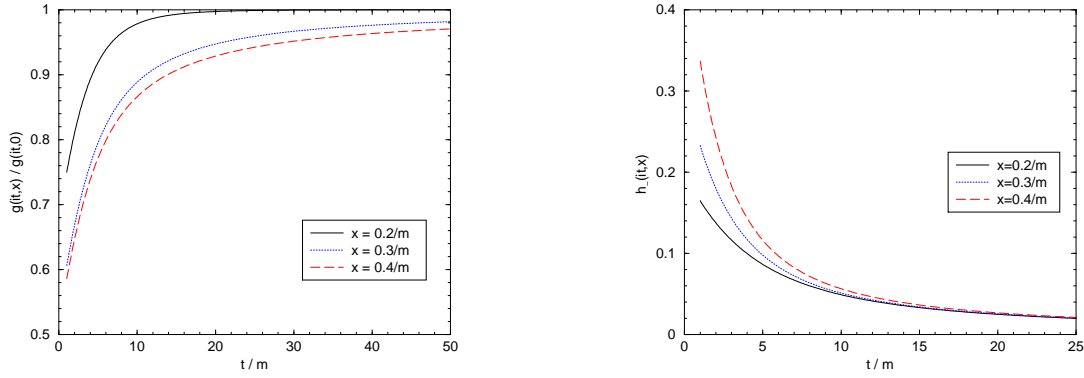


Figure 5: Plots of $g(it, x)/g(it, 0)$ and $h_-(it, x)$ as functions of the imaginary momentum t at several positions x . The parameters are $a = 0.3/m$, $w = 0.03/m$ and $\lambda = 3m$.

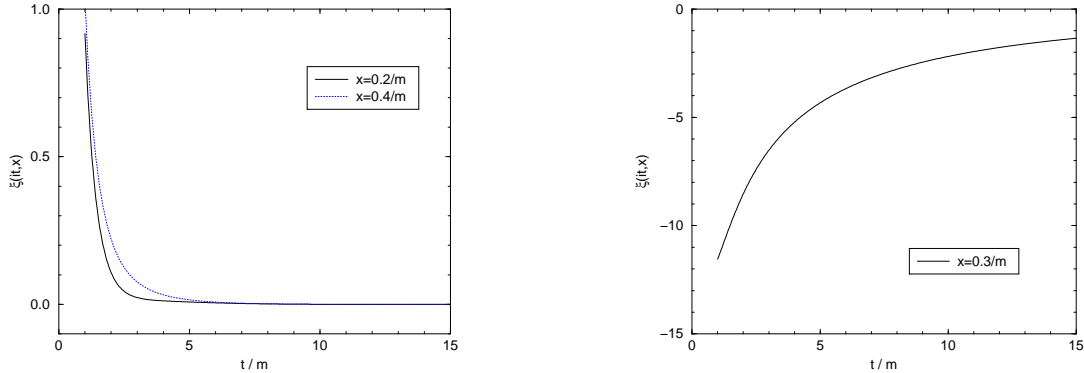


Figure 6: The Born subtracted weight function $\eta(it, x)$ for the Gaussian background field, eq. (83), as function of the imaginary momentum t at several positions x . The parameters are $a = 0.3/m$, $w = 0.03/m$ and $\lambda = 3m$.

clearly in Fig 5. By the same argument, we expect the ratio $g(it, x)/g(it, 0)$ to approach one at large t , which is confirmed in Fig 5. The functions required for the symmetric channel behave similarly. The Born subtracted continuum contribution to the energy density can be written in the form of eq. (77), where now $\eta(it, x)$ is computed numerically from $g(it, x)$ and $h_{\pm}(it, x)$. In Fig. 6 we plot $\eta(it, x)$ for the Gaussian background for several values of x . Since σ is nonzero everywhere, η falls like $1/t^3$ at large t for all x . We see that the contribution for $|x \pm a| \gg w$, where the potential σ is very small, is much smaller than the contribution from $x \approx a$, where the potential is peaked.

The energy density we obtain for a tall, narrow Gaussian is shown in Fig. 7, together with the result from the previous subsection for the δ -function background. The latter case also has a δ -function contribution to the energy, which is not shown. For $|x - a| \gtrsim 3w$ the energy densities for these two background fields are indistinguishable. For $|x - a| \lesssim 3w$ the energy density for the Gaussian background becomes dominated by a strongly peaked contribution proportional to $\sigma(x)$ (approximating the δ -function contribution).

Finally, as a check on our numerical calculation, we have verified that the total energy computed directly from eq. (67) agrees with the spatial integral of the energy density.

4. An Example in Two Space Dimensions

Our numerical methods become particularly valuable as we move to higher dimensions. Our renormalization procedure and numerical methods allow us to study a sequence of sources and examine the behavior of the energy and energy density as one attempts to take the boundary condition limit. In two dimensions we still only need the renormalization counterterm proportional to $\sigma(\vec{x})$. To go on to three dimensions would require an additional Born subtraction and a counterterm proportional to $\sigma(\vec{x})^2$.

We begin by discussing some peculiarities of the differential equations (25) and (27) for the auxiliary radial functions g_{ℓ} and h_{ℓ} necessary to handle the s -wave in two dimensions. Then we describe the computation of the total energy and energy density for a Gaussian background

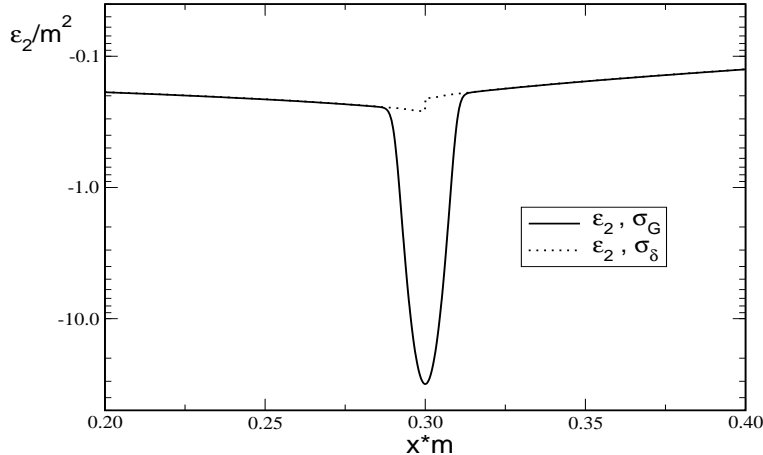


Figure 7: Comparison of the energy densities for a narrow Gaussian, σ_G with $w = 0.003/m$, and a δ -function background, σ_δ , located at $a = 0.3/m$. The coupling is $\lambda = 3m$. Note that we have omitted the $\delta(x - a)$ piece for σ_δ . Its coefficient is such that when it is added to the dotted line the areas under both curves are equal.

of width w centered on a circle of radius a , which illustrates our general conclusions about the nature of the Casimir problem.

4.1 Boundary Conditions for Radial Functions

In two space dimensions the angular momentum ℓ can be restricted to $\ell \geq 0$ with degeneracy $N_\ell = 2$ for $\ell \neq 0$ and $N_\ell = 1$ for $\ell = 0$.⁶ In each channel with $\ell > 0$, we can solve the radial problem by following the steps described in Section 2.2. Specifically, $\nu \equiv \ell - 1 + \frac{n}{2} = \ell$ and

$$\xi_\ell(z) = -\frac{d}{dz} \ln(\sqrt{z} K_\ell(z)) = \frac{\ell - \frac{1}{2}}{z} + \frac{K_{\ell-1}(z)}{K_\ell(z)} \quad (\ell \geq 0), \quad (84)$$

where $K_{-1} \equiv K_1$. These functions are smooth for positive arguments $z > 0$ and quickly approach unity for $z \gg 1$. For $\ell > 0$ they have a simple pole at $z = 0$, $\xi_\ell(z) \simeq (\ell - \frac{1}{2})/z$. However, the functions g_ℓ and h_ℓ are regular near $r = 0$,

$$g_\ell(it, r) = g_\ell(it, 0) + \mathcal{O}(r^2) \quad h_\ell(it, r) = r + \mathcal{O}(r^3) \quad (85)$$

canceling the potential singularities at $r = 0$ in eqs. (25) and (27) coming from $\xi_\ell(z)$.

For $\ell = 0$ it appears from eqs. (23) and (24) that both h_0 and the Green's function G_0 become ill-defined for $\nu = \ell = 0$. Ultimately, the source of the problem can be traced to the subleading logarithmic term in the Bessel functions,

$$w_0(kr) = i\sqrt{\frac{\pi}{2}} kr H_0^{(1)}(kr) \quad \text{and} \quad \xi_0(z) = -\frac{1}{2z} - \frac{1}{z \ln z} + \mathcal{O}(z). \quad (86)$$

⁶In the formula for N_ℓ , given after eq. (9), we first have to take $\ell = 0$ and *subsequently* $n \rightarrow 2$ for the proper treatment of the singularity in $\Gamma(n + \ell - 2)$ for this case [23].

The subleading term shows up as a singularity in $\xi'_0(z)$, while it is harmless in $\xi_0(z)$ itself. The solution is to integrate the differential equation (25) for g_0 from $r = \infty$ down to a point arbitrarily close to $r = 0$ and then get $g_0(it, 0)$ from eq. (85).

For the regular solution, we simply omit the normalization $1/2\nu$ in the *ansatz* (23) and set

$$\phi_0(k, r) = \frac{\sqrt{k}h_0(k, r)}{w_0(kr)}. \quad (87)$$

Then eq. (24) becomes

$$G_0(r, r, k) = \frac{g_0(k, r)h_0(k, r)}{g_0(k, 0)}. \quad (88)$$

The resulting differential equation for h_0 is still eq. (27), but the boundary conditions at $r = 0$ must be modified: It is straightforward to verify that

$$h_0(it, r) = -r \ln tr \quad \text{and} \quad h'_0(it, r) = -[1 + \ln tr] \quad \text{as} \quad r \rightarrow 0 \quad (89)$$

removes⁷ all small r singularities in eq. (27). We use eq. (89) to integrate the differential equation (27) numerically starting at an arbitrarily small but nonzero value r .

It is then also straightforward, although tedious, to expand g_ℓ and h_ℓ in powers of the background field σ according to eq. (31). We thus obtain the Born subtracted local spectral density, eq. (14), for each angular momentum quantum number ℓ .

The final computational ingredient in eq. (16) is the renormalized contribution from the Feynman diagrams. In two space dimensions one Born subtraction suffices. Then we have to add back in the two Feynman diagrams in Fig. 2. In the no-tadpole renormalization scheme the local diagram, eq. (38), is exactly canceled by the counterterm and we only need to add back the two-point contribution, eq. (41). The corresponding Feynman parameter integral is readily computed to be

$$\epsilon_{\text{FD}}(r) = \frac{m^2 r}{16\pi} \int_0^\infty dp J_0(pr) \tilde{\sigma}(p) \left[p + \frac{p^2 - 4m^2}{2m} \arctan \frac{p}{2m} \right], \quad (90)$$

where

$$\tilde{\sigma}(p) = 2\pi \int_0^\infty dr r J_0(pr) \sigma(r). \quad (91)$$

4.2 Numerical Results for a Gaussian Background Field

We now apply this method and discuss the numerical results for the total energy and energy density of a Gaussian background field in two dimensions. We consider

$$\sigma(r) = \lambda A e^{-\frac{(r-a)^2}{2w^2}}. \quad (92)$$

⁷The logarithmic behavior is actually expected from the free solution: $rI_0(tr)K_0(tr) \rightarrow \ln 2 - \gamma - r \ln(tr)$ as $r \rightarrow 0$, *cf.* eq. (31).

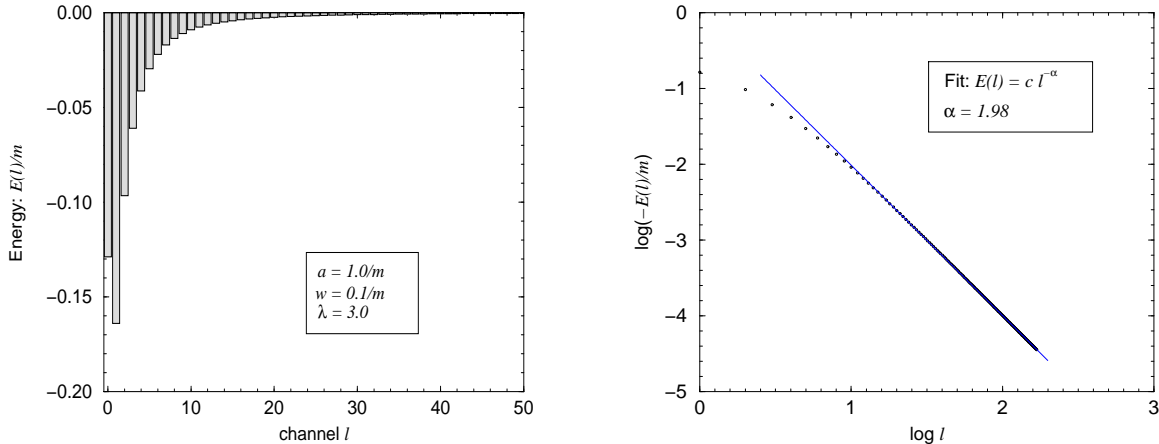


Figure 8: Contributions $E_\ell(\lambda, a, w)$ to the total energy from various angular momentum channels ℓ . The logarithmic plot on the right is consistent with the asymptotic behavior $E_\ell \sim 1/\ell^2$. The parameters are $a = 1.0/m$, $w = 0.1/m$ and $\lambda = 3m$.

This profile describes a ring of radius a and thickness w . The normalization A is chosen such that $\int_0^\infty \sigma(r)dr = \lambda$, giving $\sigma(r) \rightarrow \lambda\delta(r - a)$ as $w \rightarrow 0$. Sending the coupling strength λ to infinity subsequently imposes the Dirichlet boundary condition on a circle of radius a .

We first discuss the total energy $E[\sigma] = E(\lambda, a, w)$ computed from eq. (50). Note that no Feynman diagram contribution has to be added to the total energy because in the no-tadpole scheme $E_{\text{FD}}^{(1)} + E_{\text{CT}} = 0$. Fig. 8 shows the total energy contribution $E_\ell(\lambda, a, w)$ of the angular momentum channel ℓ , for a Gaussian ring of radius $a = 1.0/m$ and width $w = 0.1/m$. Note that the $\ell = 0$ channel is suppressed relative to $\ell > 0$ by the degeneracy factor $N_0/N_\ell = \frac{1}{2}$. Unlike the case in three dimensions, however, higher angular momentum channels are *not* favored by a further increasing degeneracy, so the contributions decay rapidly with increasing $\ell \geq 1$. The largest contribution always comes from $\ell = 1$. The logarithmic plot in Fig. 8 confirms that the asymptotic region is reached quickly and that the decay of the individual contributions is consistent with $E_\ell \propto 1/\ell^2$ for $\ell \geq 5$. While this clearly shows the finiteness of the renormalized quantum energy (for fixed a and w), the convergence is too slow to allow us to sum the ℓ -series directly. Instead, we use a speedup technique related to Richardson's approach [24], which is particularly powerful in the present case, where the asymptotic behavior sets in quickly. We have checked that the results of this method are very robust and independent of the details of the extrapolation technique used. A sufficiently high precision in the energy and density calculation can then be achieved by using only approximately 30 channels. For details on this summation technique, see Appendix C.

The computation of the total energy can be sped up even further by subtracting the second Born approximation in eq. (16) and adding back the corresponding second-order Feynman diagram. With this (over-)subtraction, the large ℓ behavior of $E_\ell(\lambda, a, w)$ changes to $1/\ell^3$. The relevant Feynman diagram is easily computed,

$$E_{\text{FD}}^{(2)}[\sigma] = \frac{1}{32\pi^2} \int_0^\infty dp \tilde{\sigma}(p)^2 \arctan \frac{p}{2m} \quad (93)$$

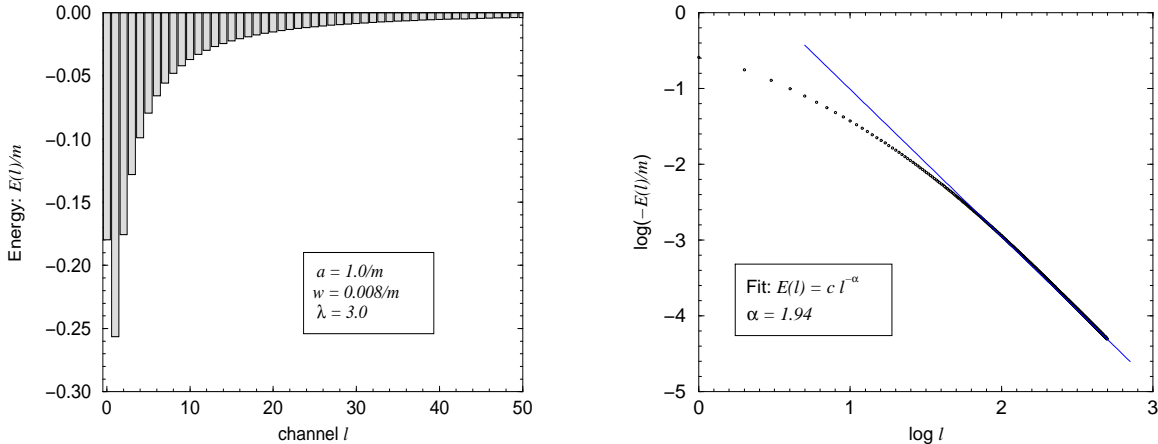


Figure 9: Contributions E_ℓ to the total energy from various angular momentum channels ℓ . The Gaussian background is much narrower than in Fig. 8 and the asymptotic decay $E_\ell \sim 1/\ell^2$ is reached for much larger channels ℓ only. The parameters are $a = 1.0/m$, $w = 0.008/m$ and $\lambda = 3m$.

where $\tilde{\sigma}$ denotes the Fourier transform, eq. (91). We have verified that this method gives the same result as before.

As the background field approaches a δ -function we find by explicit numerical calculation that the total Casimir energy diverges. To illustrate the problem we consider a very narrow configuration with $w = 0.008/m$. As can be seen by comparing Figs. 9 and 8, E_ℓ decreases more slowly with ℓ when w is smaller. For any finite width w the energy contributions E_ℓ eventually decrease steeply enough to yield a convergent sum and a finite total energy, but this asymptotic regime is only reached for much larger ℓ when the width is small. This is a typical non-uniform behavior: For any fixed width, there is always a channel ℓ_0 large enough such that the energies E_ℓ decay as $1/\ell^2$ for $\ell \geq \ell_0$. On the other hand, for every fixed channel ℓ we can always find a width w small enough such that we are far from the asymptotic region. Eventually, as $w \rightarrow 0$ the asymptotic region is never reached and the total energy diverges.

One can also understand this divergence in terms of the second Born approximation, which we separated out in the oversubtraction procedure above. For the singular background, $\sigma(r) = \lambda\delta(r - a)$, this diagram contributes

$$E_{\text{FD}}^{(2)}[\lambda\delta(r - a)] = \frac{\lambda^2 a^2}{8} \int_0^\infty dp J_0^2(ap) \arctan \frac{p}{2m} \quad (94)$$

which diverges logarithmically at large p just as the sum over channels did without oversubtraction. Oversubtraction shifts the divergence from the ℓ sum into the momentum integral in the Feynman diagrams. Whichever choice we make, the divergence cannot be renormalized away, despite the claims of [12]; it is a physical effect. Its implications for the usual Casimir calculations will be studied elsewhere [7].

Next we examine the radial energy density $\epsilon(r)$. As a numerical check, we have verified that its integral over r agrees with the total energy computed directly from eq. (50). In Fig. 10

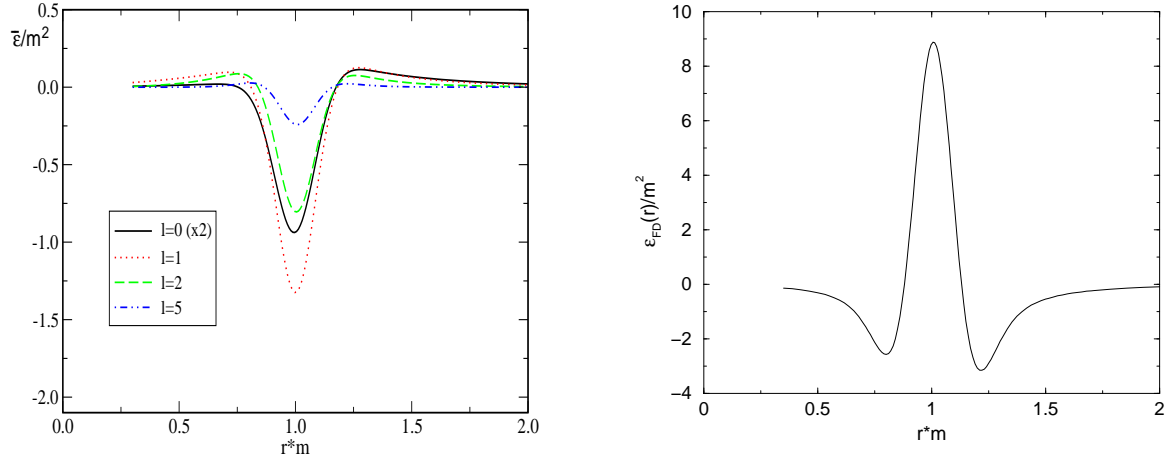


Figure 10: Left panel: Contributions of various angular momentum channels to the Born subtracted energy density $\bar{\epsilon}(r)$. Note that we have multiplied the $\ell = 0$ contribution by a factor of 2 to better display the secular decrease with ℓ . Right panel: The Feynman diagram contribution $\epsilon_{FD}(r)$. The parameters for both panels are $a = 1.0/m$, $w = 0.1/m$ and $\lambda = 3m$. See also Fig. 11 for the total energy density $\epsilon(r)$ found by combining the components displayed here.

we display the contributions of various angular momentum channels to the Born subtracted energy density, $\bar{\epsilon}(r)$, for a relatively wide profile, $w = 0.1/a$. Generically the contributions to the energy density from various angular momentum channels vary in magnitude but have similar radial shapes. As for the total energy, the $\ell = 0$ channel is suppressed by a degeneracy factor $1/2$; the largest contribution comes from $\ell = 1$ with all higher channels decaying quickly with increasing ℓ . For narrower widths the decay with ℓ is slower, as we expect from the preceding discussion of the total energy. The smooth asymptotic behavior allows us again to use an extrapolation method in order to speed up the sum over channels.

Figure 10 also shows the renormalized Feynman diagram contribution in the right panel. Since the integral over all radii r is zero, the peak at the location of the background profile must be compensated by negative densities on both sides. The sign and width of the peak essentially reproduce the Gaussian background itself, while the similar peak in the density $\bar{\epsilon}(r)$ has the opposite sign and reduces the overall magnitude of the density. As can be seen from the total energy density $\epsilon(r)$ in Fig. 11, combining all the contributions still yields a pronounced peak at the location of the background. As we decrease the width of $\sigma(r)$, the peak increases in magnitude and becomes narrower. In the δ -function limit it develops a non-integrable singularity, unlike the case in one dimension.

Figs. 11 and 12 display the dependence of the energy density for various values of r on the width of the Gaussian background field. We see the non-uniform approach to the limit $w \rightarrow 0$. In particular, it is clear that the energy density approaches a finite limit at any fixed r as $w \rightarrow 0$, even though the limiting function diverges as $r \rightarrow a$. Sufficiently far away from the location of the Gaussian, around $|r - a| \gtrsim 3w$, the energy density quickly approaches the limiting form, corresponding to that of a δ -function background. In contrast, at $r = a$, no such limiting value exists. This behavior can also be seen in Fig. 12, where we display

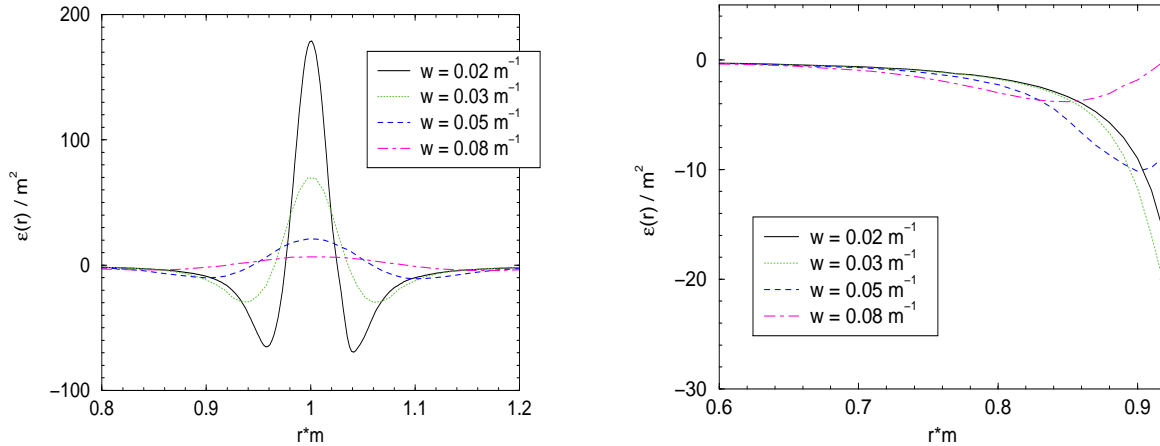


Figure 11: The energy density in units of m^2 for the Gaussian background field located at $a = 0.1/m$ with strength $\lambda = 3.0m$ for various values of the width w . The left panel shows the energy density for all radii. The right panel focuses on the region where the densities can be seen to converge toward the limiting form.

the energy density at various values of r as function of the width. The limiting form is approached more rapidly the farther one is away from the Gaussian peak.

The Dirichlet boundary condition is achieved only by taking $\sigma(r) \rightarrow \lambda\delta(r-a)$, followed by the limit $\lambda \rightarrow \infty$. However, since the renormalized Casimir energy diverges as σ approaches a δ -function, it is impossible to define the Casimir energy for any sharp background field, much less one with infinite coupling. Thus the Dirichlet–Casimir energy of a circle in two dimensions does not exist. But all is not lost: the energy density away from the source approaches a finite limit as the background becomes sharp.

5. Summary and Outlook

In this paper we have developed an efficient method to compute one-loop energies and energy densities in renormalizable quantum field theories. Starting from a Green’s function formalism, we employ Born subtractions to implement definite renormalization conditions, and express the result in a form that allows for direct, efficient calculation after analytic continuation to the imaginary k axis. This method allows us to study the limit in which smooth background fields approach idealized boundary conditions, illuminating subtleties of the process by which standard Casimir calculations are realized in renormalized quantum field theory. We find that although the Casimir force between rigid bodies and energy densities away from the boundaries are well-defined observables, quantities like the Casimir energy have divergences that cannot consistently be renormalized. These divergences have physical consequences in examples such as the stress on a circle, where we have to compare two configurations for which the divergent contributions differ. In these cases, the physical effects depend strongly on the details of the source.

We have also shown rigorously that the total energy, as obtained from the integrated energy density, can be expressed as the integral over single particle energies weighted by the

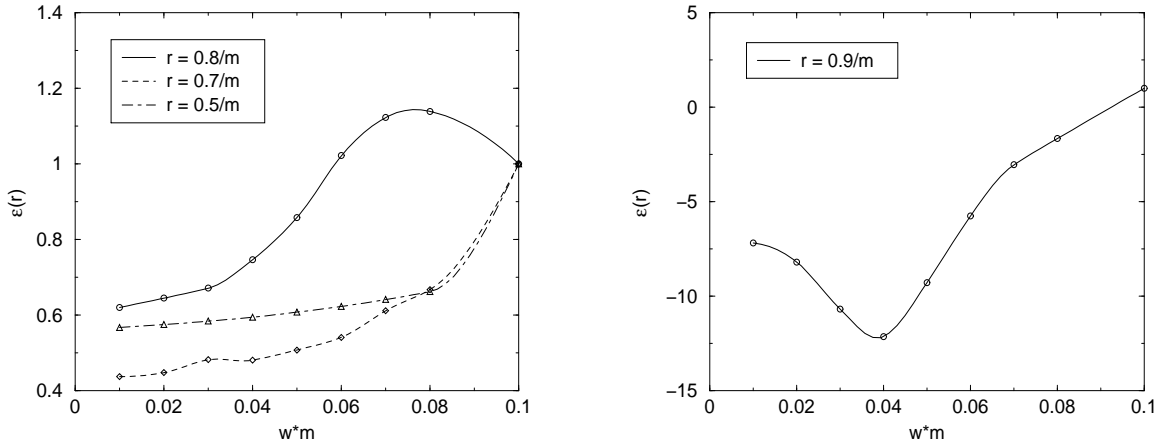


Figure 12: The energy density of the Gaussian background field located at $a = 1.0/m$ and with strength $\lambda = 3.0m$. The figure shows the energy densities at various values of r as functions of the width, w . The densities are scaled to $\epsilon(r)$ at $w = 0.1/m$.

change in the density of states, which is given by the derivative of the phase shifts.

There are many possible applications of our method. It can be generalized to fermions [25] and to situations where the energy spectrum is asymmetric about zero. In the latter case we would have to add the different contributions from the two sides of the cut in Fig. 1. In such systems the background field can carry nonzero charge density, since the contribution to the charge density from positive and negative energy modes will no longer cancel. It could also be calculated with our approach. We could consider the electromagnetic field in the presence of conductors by decomposing it into a scalar field obeying Neumann boundary conditions plus a scalar field obeying Dirichlet boundary conditions. We have seen in this paper how to implement Dirichlet boundary conditions with a background potential, and the Neumann boundary condition can be treated in a similar way [26]. Therefore we are equipped to reconsider problems such as the surface tension of a conducting sphere in QED [8]. Our calculational method is well suited to soliton calculations, generalizing [27] beyond the case of reflectionless potentials. Finally, in cases like the Gross–Neveu or Nambu–Jona–Lasinio models, where one introduces the background potential as a non-dynamical auxiliary field coupled to a dynamical field, one can search for solitons as self-consistent solutions to the auxiliary field equations of motion [28, 29]. These equations of motion are obtained by first integrating out the dynamical field, leaving an effective action for the auxiliary field. This procedure generates expressions involving the full Green’s function similar to those we have considered here, which could be computed efficiently with our methods.

Acknowledgments

We gratefully acknowledge discussions with E. Farhi and K. D. Olum. N. G. and R. L. J. are supported in part by the U.S. Department of Energy (D.O.E.) under cooperative research agreements #DE-FG03-91ER40662 and #DF-FC02-94ER40818. M. Q. and H. W. are supported by the Deutsche Forschungsgemeinschaft under contracts Qu 137/1-1 and We 1254/3-2.

Appendix A: Density of States and the Jost Function

In this Appendix, we demonstrate the relation (48) between the integral over r of the local spectral density and the Jost function

$$2 \int_0^\infty dr [\rho_\ell(k, r)]_0 = \frac{2k}{i} \int_0^\infty dr [G_\ell(r, r, k) - G_\ell^{(0)}(r, r, k)] = i \frac{d}{dk} \ln F_\ell(k), \quad (\text{A.1})$$

which is valid everywhere in the upper half-plane $\text{Im } k > 0$. This formula can be used both to establish an efficient computation of the total energy on the imaginary axis, and also to relate the density of states for real k to the phase shift.

We start by differentiating the Wronskian of the Jost solution, $f_\ell(k, r)$, and the regular solution, $\phi_\ell(k', r)$ [30],

$$\frac{d}{dr} W[f_\ell(k, r), \phi_\ell(k', r)] = (k^2 - k'^2) f_\ell(k, r) \phi_\ell(k', r) \quad (\text{A.2})$$

where all quantities in this relation are analytic for $\text{Im } k > 0$. We integrate both sides from $r = 0$ to $r = R$. Since the regular solution $\phi_\ell(k, r)$ becomes k -independent at small r , we can compute the boundary term at $r = 0$ by replacing k' with k and using the standard Wronskian,

$$W[f_\ell(k, r), \phi_\ell(k, r)] = (-k)^{\frac{1}{2}-\nu} F_\ell(k), \quad (\text{A.3})$$

giving

$$W[f_\ell(k, R), \phi_\ell(k', R)] = (-k)^{\frac{1}{2}-\nu} F_\ell(k) + (k^2 - k'^2) \int_0^R dr f_\ell(k, r) \phi_\ell(k', r). \quad (\text{A.4})$$

Next we differentiate with respect to k , set $k' = k$, and use the representation (22) for the Green's function to obtain

$$\frac{(-k)^{\nu-\frac{1}{2}}}{F_\ell(k)} W[\dot{f}_\ell(k, R), \phi_\ell(k, R)] = \frac{\nu - \frac{1}{2}}{k} + \frac{\dot{F}_\ell(k)}{F_\ell(k)} + 2k \int_0^R dr G_\ell(r, r, k), \quad (\text{A.5})$$

where $\dot{f}_\ell(k, R) \equiv \frac{d}{dk} f_\ell(k, R)$ and $\dot{F}_\ell(k) \equiv \frac{d}{dk} F_\ell(k)$. To eliminate the first term on the right-hand side, we subtract the same equation for the non-interacting case, giving

$$\begin{aligned} & \frac{(-k)^{\nu-\frac{1}{2}}}{F_\ell(k)} W[\dot{f}_\ell(k, R), \phi_\ell(k, R)] - (-k)^{\nu-\frac{1}{2}} W[\dot{f}_\ell^{(0)}(k, R), \phi_\ell^{(0)}(k, R)] \\ &= \frac{\dot{F}_\ell(k)}{F_\ell(k)} + 2k \int_0^R dr [G_\ell(r, r, k) - G_\ell^{(0)}(r, r, k)]. \end{aligned} \quad (\text{A.6})$$

To complete the proof, we have to show that the left hand side of eq. (A.6) vanishes as $R \rightarrow \infty$. To see this, we write the boundary condition (18) for the Jost solution in the form

$$f_\ell(k, R) = w_\ell(kR) [1 + \mathcal{O}(R^{-1})], \quad R \rightarrow \infty \quad (\text{A.7})$$

which can also be inferred from the integral equation obeyed by $f_\ell(k, r)$. Differentiating with respect to k and using the asymptotics of the free Jost solution $w_\ell(kR)$,

$$\dot{w}_\ell(kR) = \frac{d}{dk} w_\ell(kR) = iR w_\ell(kR) \left[1 + \mathcal{O}(R^{-2})\right],$$

it is easy to show the asymptotic behavior

$$\dot{f}_\ell(k, R) = iR f_\ell(k, R) \left[1 + \mathcal{O}(R^{-2})\right]. \quad (\text{A.8})$$

The first term on the left-hand side of eq. (A.6) can thus be estimated by

$$\begin{aligned} & \frac{(-k)^{\nu-\frac{1}{2}}}{F_\ell(k)} W[f_\ell(k, R), \phi_\ell(k, R)] = \\ & \left\{ iR \frac{(-k)^{\nu-\frac{1}{2}}}{F_\ell(k)} W[f_\ell(k, R), \phi_\ell(k, R)] - i \frac{(-k)^{\nu-\frac{1}{2}}}{F_\ell(k)} f_\ell(k, R) \phi_\ell(k, r) \right\} \left[1 + \mathcal{O}(R^{-2})\right] \\ & = -i [R + G_\ell(R, R, k)] \left[1 + \mathcal{O}(R^{-2})\right], \end{aligned} \quad (\text{A.9})$$

where we have used the Wronskian of f_ℓ and ϕ_ℓ and the definition of the Green's function, eq. (22). Subtracting the analogous equation in the free case, the term proportional to R drops out and we are left with

$$\begin{aligned} & \frac{(-k)^{\nu-\frac{1}{2}}}{F_\ell(k)} W[f_\ell(k, R), \phi_\ell(k, R)] - (-k)^{\nu-\frac{1}{2}} W[f_\ell^{(0)}(k, R), \phi_\ell^{(0)}(k, R)] \\ & = -i [G_\ell(R, R, k) - G_\ell^{(0)}(R, R, k)] \left[1 + \mathcal{O}(R^{-1})\right]. \end{aligned} \quad (\text{A.10})$$

We estimate the large- R behavior of the difference $\Delta_\ell(k, R) \equiv G_\ell(R, R, k) - G_\ell^{(0)}(R, R, k)$ from eqs. (A.9) and (A.6),

$$-i \Delta_\ell(k, R) \left[1 + \mathcal{O}(R^{-1})\right] = \frac{\dot{F}_\ell(k)}{F_\ell(k)} + 2k \int_0^R dr \Delta_\ell(k, r). \quad (\text{A.11})$$

It is then straightforward to solve for $\Delta_\ell(k, R) \simeq i [C_\ell(k) + \mathcal{O}(1)R] \exp(2ikR)$ at large R , where $C_\ell(k)$ is an R -independent integration constant. The left-hand side vanishes exponentially for all $\text{Im } k > 0$ as $R \rightarrow \infty$, so in this limit we obtain eq. (A.1), which completes the proof.

It is also instructive to explore the consequences of this result on the real axis. If we let k approach the real axis from above, we see that to leading order in R^{-1} , the integral equation (A.11) allows for a solution going like $R \exp[2ikR]$, which violates the bounds in eq. (30) if k is real. Thus the coefficient of this term must actually be zero, leaving

$$\frac{\dot{F}_\ell(k)}{F_\ell(k)} + 2k \int_0^R dr [G_\ell(r, r, k) - G_\ell^{(0)}(r, r, k)] = C_\ell(k) \exp(2ikR) \left[1 + \mathcal{O}(R^{-1})\right] \quad (\text{A.12})$$

which oscillates as $R \rightarrow \infty$ when k is real. As is typical for continuum problems, we must specify that the limit where k becomes real is taken after the integral over r to eliminate the contribution from these oscillations at the upper limit of integration.

On the real axis, we can relate the Jost function to the phase shift by eq. (52). Taking the imaginary part of eq. (A.1) and using eq. (54) yields the relationship between the density of states and the phase shift,

$$\frac{1}{\pi} \frac{d\delta_\ell}{dk} = \frac{2k}{\pi} \text{Im} \int_0^\infty \left(G_\ell(r, r, k + i\epsilon) - G_\ell^{(0)}(r, r, k + i\epsilon) \right) dr = \rho_\ell(k) - \rho_\ell^{(0)}(k). \quad (\text{A.13})$$

We can also rewrite eq. (A.13) as

$$\frac{2}{\pi} \int_0^\infty dr \left(\psi_\ell^*(k, r) \psi_\ell(k, r) - \psi_\ell^{(0)*}(k, r) \psi_\ell^{(0)}(k, r) \right) = \frac{1}{\pi} \frac{d\delta_\ell}{dk} \quad (\text{A.14})$$

where the momentum on the left-hand side is understood to be defined with the $i\epsilon$ prescription to eliminate the contribution from the oscillations of the wavefunctions at spatial infinity.

Appendix B: Two Jost functions in One Dimension

In this Appendix, we discuss a technique special to one dimension, which applies even when the background field is not symmetric. Scattering in one dimension can be described in terms of two Jost solutions $f_\pm(k, x)$, which obey the boundary conditions

$$\lim_{x \rightarrow \pm\infty} f_\pm(k, x) e^{\mp ikx} = 1. \quad (\text{B.1})$$

The Green's function then is

$$G(x, y, k) = i \frac{T(k)}{2ik} f_+(k, x_>) f_-(k, x_<), \quad (\text{B.2})$$

where $T(k)$ is the transmission coefficient. For numerical computations it is convenient to factor exponentials out of $f_\pm(k, x)$. We define

$$g_\pm(k, x) = e^{\mp ikx} f_\pm(k, x), \quad (\text{B.3})$$

which obey the differential equations

$$-g_\pm''(it, x) \pm 2tg_\pm'(it, x) + \sigma(x)g_\pm(it, x) = 0 \quad (\text{B.4})$$

with the boundary conditions

$$\lim_{x \rightarrow \pm\infty} g_\pm(it, x) = 1 \quad \text{and} \quad \lim_{x \rightarrow \pm\infty} g_\pm'(it, x) = 0, \quad (\text{B.5})$$

and are bounded in the upper half k -plane. The Green's function for equal arguments then reads

$$G(x, x, it) = \frac{T(it)}{2t} g_+(it, x) g_-(it, x). \quad (\text{B.6})$$

The transmission coefficient is most conveniently computed using the Wronskian for f_{\pm} , yielding

$$G(x, x, it) = \frac{g_+(it, x)g_-(it, x)}{g'_+(it, 0)g_-(it, 0) - g'_-(it, 0)g_+(it, 0) + 2tg_+(it, 0)g_-(it, 0)}, \quad (\text{B.7})$$

for the Green's function at equal spatial arguments. In this form, we can compute the Green's function without encountering any oscillatory or exponentially growing contributions.

Appendix C: Slowly Convergent Series

In the examples studied in the main text, the sum over angular momentum channels ℓ is slowly converging, typically going as $1/\ell^2$ for large ℓ . From a numerical point of view, such a decay is too slow for a direct summation as it requires to compute $\mathcal{O}(1000)$ channels to get a relative precision of 1%. Even worse, the narrow Gaussian profiles relevant for Casimir problems have a tendency to fall like $1/\ell$ before they eventually turn over to a $1/\ell^2$ behavior at channels with large angular momenta, $\ell \geq \ell_0 \gg 1$.

To sum such series efficiently using only a small number of channels, we employ a technique related to Richardson's method [24]. Given a slowly converging sum $\sum_{\ell=0}^{\infty} a_{\ell}$, we define a function $f(t)$ at the particular points t_n by

$$f(t_n) \equiv \sum_{\ell=0}^n a_{\ell}, \quad t_n \equiv \frac{1}{n+1} \quad (n = 0, 1, 2, \dots) \quad (\text{C.1})$$

which gives the value of the full infinite series in the limit $t \rightarrow 0$. We assume that $f(0)$ can be approximated by a smooth extrapolation using the points t_n , which accumulate around $t = 0$. Thus given values a_0, \dots, a_N from the first $N+1$ channels, we construct an interpolating function \tilde{f} of a fixed order ν through the last $\nu+1$ points $t_N, t_{N-1}, \dots, t_{N-\nu}$ (for the first few channels $N < \nu$, so in those cases we take $\nu = N$). The extrapolation to $t = 0$ gives an approximation $\tilde{f}(0)$ for the sum of the series and an error estimate based on the assumption of a smooth underlying function $f(t)$. While new channels are computed, we monitor $\tilde{f}(0)$ and terminate if we have a satisfying error estimate. For our purposes, the best results are obtained from a rational function (or Padé) approximation, since the resulting $\tilde{f}(t)$ has the tendency to anticipate the smooth behavior of the underlying $f(t)$. To illustrate the method, let us look at the example

$$\sum_{\ell=1}^{\infty} \frac{\ell_0}{\ell(\ell + \ell_0)} \quad (\text{C.2})$$

which imitates the behavior of our typical sums over channels: It starts with $a_{\ell} \sim 1/\ell$ and turns into the converging $1/\ell^2$ behavior for $\ell > \ell_0$. In the table below, we show the results of our method with the standard parameters used in the main text. We also give the number of channels actually summed and compare with the results obtained by direct summation of the same number of channels.

As we can see from the table, our method improves the accuracy dramatically. For small turning points ℓ_0 , the first 10 channels are sufficient to find the exact value. As we go to

Table C.1: Results of our extrapolation method as compared to direct summation for the test series eq. (C.2).

ℓ_0	5	10	50	500	1000	5000	10000
exact	2.2833	2.9290	4.4992	6.7928	7.4855	9.0945	9.7875
interpol.	2.2833	2.9290	4.4949	6.7385	7.3077	8.0560	8.2627
<i>error [%]</i>	$2.2 \cdot 10^{-6}$	$2.38 \cdot 10^{-5}$	0.095	0.80	2.37	11.4	15.6
direct	1.8941	2.2602	2.7483	3.9672	4.1653	4.2706	4.3684
<i>error [%]</i>	17.0	22.8	38.9	41.6	44.4	53.0	55.3
channels	10	10	10	31	37	40	44

higher ℓ_0 , it becomes more difficult to predict the exact result from the lowest terms which do not yet see the asymptotic decay. Even then, with ℓ_0 as large as 500, we can still achieve a precision of $< 1\%$ using the first $\mathcal{O}(30)$ channels only. The direct summation is off by more than 40% in this case. Eventually, for very large $\ell_0 \simeq 10000$, the error of the Padé approximation increases up to 15%. This is not too surprising since there is no trace of the eventual $1/\ell^2$ decay in the first 44 channels summed. In order to predict the correct result within 1% for the case $\ell_0 = 10000$, our method would in fact have to use $\mathcal{O}(400)$ channels (but the direct summation would still be off by $> 30\%$ in this case).

References

- [1] H. B. G. Casimir, Kon. Ned. Akad. Wetensch. Proc. **51** (1948) 793.
- [2] A. A. Grib, S. G. Mamayev and V. M. Mostepanenko, *Vacuum Quantum Effects in Strong Fields*, St. Petersburg, 1994.
- [3] V.M. Mostepanenko and N.N. Trunov, *The Casimir Effect and its Applications*, Clarendon Press, Oxford (1997), M. Bordag, U. Mohideen and V. M. Mostepanenko, Phys. Rept. **353** (2001) 1 [arXiv:quant-ph/0106045],
- [4] K. A. Milton, *The Casimir Effect: Physical Manifestations Of Zero-Point Energy*, World Scientific (2001).
- [5] G. Plunien, B. Müller and W. Greiner, Phys. Rept. **134** (1986) 87.
- [6] M. Bordag, ed., *Proceedings of the Fifth Workshop on Quantum Field Theory Under the Influence of External Conditions*, Intl. J. Mod. Phys. **A17** (2002) No. 6 & 7.
- [7] N. Graham R.L. Jaffe, V. Khemani, M. Quandt, M. Scandurra, and H. Weigel, *Casimir Energies in the Light of Quantum Field Theory*, in preparation.
- [8] T. H. Boyer, Phys. Rev. **174** (1968) 1764.
- [9] N. D. Birrel and P. C. W. Davies, *Quantum Fields in Curved Space*, Cambridge, Cambridge University Press, 1982.
- [10] K. D. Olum and N. Graham, arXiv:gr-qc/0205134.
- [11] S. G. Mamayev and N. N. Trunov, Theor. Math. Phys. **38** (1979) 228 [Teor. Mat. Fiz. **38** (1979) 345].
- [12] K. A. Milton and Y. J. Ng, Phys. Rev. D **46** (1992) 842, S. Leseduarte and A. Romeo, Ann. Phys. **250** (1996) 448 [arXiv:hep-th/9605022].
- [13] S. Blau, M. Visser and A. Wipf, Nucl. Phys. B **310** (1988) 163.
- [14] E. Farhi, N. Graham, P. Haagensen and R. L. Jaffe, Phys. Lett. B **427** (1998) 334 [arXiv:hep-th/9802015], E. Farhi, N. Graham, R.L. Jaffe, and H. Weigel, Phys. Lett. B **475** (2000) 335 [arXiv:hep-th/9912283], Nucl. Phys. B **585** (2000) 443 [arXiv:hep-th/0003144], Nucl. Phys. B **630** (2002) 241 [arXiv:hep-th/0112217].
- [15] For a comprehensive review see: N. Graham, R. L. Jaffe and H. Weigel, Int. J. Mod. Phys. A **17** (2002) 846 [arXiv:hep-th/0201148].
- [16] M. Bordag and K. Kirsten, Phys. Rev. D **53** (1996) 5753 [arXiv:hep-th/9608070].
- [17] M. Bordag and J. Lindig, J. Phys. A **29** (1996) 4481.

- [18] N. Graham, R. L. Jaffe, M. Quandt and H. Weigel, Phys. Rev. Lett. **87** (2001) 131601 [arXiv:hep-th/0103010].
- [19] N. Graham, R. L. Jaffe, M. Quandt and H. Weigel, Ann. Phys. **293** (2001) 240 [arXiv:quant-ph/0104136].
- [20] M. Bordag, J. Phys. A **28** (1995) 755.
- [21] K. Chadan and P.C. Sabatier, *Inverse Problems in Quantum Scattering Theory*, Springer-Verlag (1977).
- [22] J. Baacke and S. Junker, Phys. Rev. D **49** (1994) 2055 [arXiv:hep-ph/9308310].
- [23] E. Farhi, N. Graham, R. L. Jaffe and H. Weigel, Nucl. Phys. B **595** (2001) 536 [arXiv:hep-th/0007189].
- [24] H. Press et. al., *Numerical Recipes in C++, 2nd edition*, Cambridge University Press (2002).
- [25] P. Sundberg and R. L. Jaffe, in preparation.
- [26] E. Farhi, private communication.
- [27] A. S. Goldhaber, A. Litvintsev and P. van Nieuwenhuizen, arXiv:hep-th/0109110.
- [28] R. Alkofer, H. Reinhardt and H. Weigel, Phys. Rept. **265** (1996) 139 [arXiv:hep-ph/9501213].
- [29] J. Baacke and H. Sprenger, Phys. Rev. D **60** (1999) 054017 [arXiv:hep-ph/9809428].
- [30] R. Newton, *Scattering Theory of Waves and Particles*, McGraw-Hill (1966), Section 12.1.